ABSTRACT

Title of Document:	SIMULATION AND MODELING OF AN ACOUSTICALLY FORCED MODEL ROCKET INJECTOR
	David Gers, Master of Science, 2010
Directed By:	Associate Professor, Kenneth H. Yu, Department of Aerospace Engineering

A numerical and experimental study was performed to assess the capability of the Loci-CHEM CFD solver in simulating dynamic interaction between hydrogen-oxygen turbulent diffusion flames and periodic pressure waves. Previous experimental studies involving a single-element shear-coaxial model injector revealed an unusual flame-acoustic interaction mechanism affecting combustion instability characteristics. To directly compare the simulation and experiments, various models in the present solver were examined and additional experiments conducted. A customized mesh and corresponding boundary conditions were designed and developed, closely approximating the experimental setup. Full 3-D simulations were conducted using a hybrid RANS/LES framework with appropriate chemistry and turbulence models. The results were compared for both reacting and non-reacting flows that were excited at various forcing frequencies representing both resonant and non-resonant behaviors. Although a good qualitative agreement

was obtained for the most part, there was a significant discrepancy in simulating the flame-acoustic interaction behavior observed under non-resonant forcing conditions.

SIMULATION AND MODELING OF AN ACOUSTICALLY FORCED MODEL ROCKET INJECTOR

By

David Michael Gers

Thesis submitted to the Faculty of the Graduate School of the
University of Maryland, College Park, in partial fulfillment
of the requirements for the degree of
Master of Science
2010

Advisory Committee:
Dr. Kenneth Yu, Chair
Dr. Chris Cadou
Dr. Arnaud Trouvé

Dedication

To my parents, for all their love and support.

Acknowledgements

I would first like to thank my advisor, Dr. Yu, for his guidance and assistance on this project and throughout my undergraduate and graduate career. I would also like to thank Dr. Trouvé for his advice and input on this project. I would especially like to thank Dr. Amardip Ghosh and Qina Diao, who provided a great deal of help throughout all phases of this research, as well as the rest of my lab mates with whom I've shared my graduate experience.

I would also like to acknowledge the funding that made this research possible. This work was sponsored by a grant from NASA CUIP. I would like to thank Joe Ruf of NASA-Marshall for his help with various aspects of this project.

Table of Contents

List of Figures and Tables

Table of Nomenclature

A	Area
B	Amplitude
c	Speed of sound
e_0	total energy of mixture
f	Frequency
F_i	Inviscid flux vector
F_v	Viscous flux vector
$\tilde{\tilde{I}}$	Identity tensor
$k_{b,r}$	Backward reaction rate
$k_{f,r}$	Forward reaction rate
L	Length
$\dot{m}$	Mass flow rate
M_s	Species atomic mass
n	Time step
NR	Number of chemical reactions
NS	Number of chemical species
$\tilde{n}$	Unit vector normal to the surface
P	Pressure
P’	Fluctuating component of pressure
Pr	Prandtl number
q	Heat release
q’	Fluctuating component of heat release
$\tilde{q}$	Heat conduction vector
Q	Vector of conservative variables
r	Radius
R_s	Species gas constant
t	Time
T	Temperature
$\tilde{u}$	Velocity vector
v	Velocity
$\dot{W}$	Chemistry source term vector
$\dot{w}$	Species chemical production rate
ρ	Density
μ	Dynamic viscosity
μ_t	Turbulent viscosity
$\tilde{\tilde{\tau}}$	Stress tensor

1. Introduction

1.1 Background and Motivation

Combustion instability has been a challenging problem in the power and propulsion community for a long time [Candel 1992]. Instability occurs when high amplitude pressure oscillations couple with in-phase heat release fluctuations [Rayleigh 1945, Culick 1987]. This can have significant effects on system performance, and can also result in damaging pressure loads and heat transfer rates, which can ultimately cause catastrophic failures. Although this problem has been studied extensively and many empirical relations have been determined, no comprehensive solutions have been discovered, and the appearance of instabilities can still derail the development of new engine designs [Hulka & Hutt 1994]. Since full-scaling testing is expensive and time-consuming, it would be very useful to have computational tools capable of predicting the development of instabilities earlier in the design process.

Combustion instabilities have been observed in many types of power and propulsion systems. In particular, liquid rocket engines have suffered from combustion instabilities throughout their development [Culick & Yang 1995]. Small amplitude pressure oscillations that naturally occur within the engine can couple with the heat release fluctuations if the phasing is correct. Principal types of instabilities that occur in rocket engines may be classified into low frequency instabilities and high frequency instabilities. Low frequency instabilities, typically of several hundred Hz or less, are usually associated with a coupling between the combustion process

and the propellant feed lines. High frequency instabilities tend to arise from the excitation of acoustic modes of the combustion chamber. High frequency instabilities are usually associated with transverse or tangential modes of the combustion chamber, and result in high amplitude oscillations on the order of kHz or higher, that can be very difficult to control. These instabilities can cause strong vibrations that can damage sensitive guidance and control components [Ebrahimi 2000], high amplitude pressure oscillations that can strain structural components [Reardon 1964, Reardon et al. 1967], and high heat release rates that can lead to destructive burnouts [Male et al. 1964].

Understanding the interaction between the acoustic waves and the flow field is especially important in the near-injector region. Atomization, mixing, and burning are all occurring in this area in the presence of strong density and velocity gradients that results from the injection of the fuel and oxidizer. For the purposes of this work, the focus will be on looking at heat release fluctuations from shear-coaxial injectors. These injectors feature a central flow of oxidizer, typically liquid oxygen, surrounded by an outer co-flow of fuel, typically hydrogen. As the LOX atomizes and mixes with the hydrogen, a turbulent diffusion flame forms at the interface. These injectors are used in a large number of rocket engines, including the space shuttle main engines.

Near these injectors there are both high velocity and density gradients present. Purely tangential modes have been shown to be problematic, especially in the higher density regions near the injector [Kim & Williams 1998]. Strong pressure and velocity gradients in this region can interact in several ways, and most of the physical

mechanisms that can cause instability are present in this near injector region [Oefelein & Yang 1997]. Since strong amplitude pressure waves are already more commonly present in this region, they can then cause oscillatory heat release via one of these mechanisms, and this can possibly in turn couple together with the acoustics and cause an increase in the amplitude of both the pressure waves and the heat release fluctuations.

Despite a long history of use and experimentation with these injectors, it is still not definitively known which of the several possible physical mechanisms is responsible for instability onset [Glogowski et al. 1994]. Factors such as velocity ratio, density ratio, fuel temperature, and combustor geometry all affect the stability limits, and although some general trends are seen, combustor design and analysis remain a very system-specific problem [Hulka & Hutt 1994]. Oftentimes instabilities will arise late in a design process, forcing either a redesign, or the addition of passive control devices such as acoustic baffles or liners. To be able to computationally predict these instabilities earlier in the design process would save both money and time during the design process, as well as assist in the analysis of existing systems that are susceptible to instability.

Over the past several decades computational fluid dynamics, or CFD, has become a useful tool in the design and development of propulsions systems. However, the ability to capture the appropriate physics needed to predict and simulate combustion instability is still a challenge. Especially important is the ability to correctly simulate the frequency, amplitude, and phase of fluctuating heat release responding to pressure oscillations. The combination of turbulence modeling,

combustion modeling, and time-dependent resolution of acoustics are all essential to capturing the proper physical mechanisms responsible for combustion instability. This work examines one specific CFD architecture of NASA's interest and uses it to model a shear-coaxial injector element under acoustic forcing, in an effort to analyze its feasibility at capturing these important flame-acoustic interactions.

1.2 Objectives and Scope

The primary objective of this work was to assess the feasibility of using the NASA CFD solver Loci-CHEM to simulate flame-acoustic interactions. Previous experimental work by Ghosh et al. (2007) examined various parameters affecting the stability of a model shear coaxial injector, and reported unusual asymmetric flame oscillations stemming from the interaction between turbulent diffusion flames and compression waves at certain frequencies. A capability to correctly simulate such flame-acoustic interaction is essential for predicting combustion instabilities, because fluctuating heat release critically affects the onset of combustion instabilities. At the time when this study was undertaken, it was not at all clear what the limitations of Loci-CHEM were and whether it would be able to capture the experimentally observed flame behavior.

The focus of this work was to simulate the experimental conditions as closely as possible and compare the results with existing database. Additional experimental data was needed to provide better validation points for the simulation results. As part of the general study investigating the capabilities of Loci-CHEM, several smaller aspects of the code were also considered. Initially, the handling of acoustics in Loci-CHEM was to be examined, and a method for creating a numerical loudspeaker using

existing boundary conditions was to be developed. Simple grid geometries could be used to verify the ability of Loci-CHEM to properly handle acoustic waves and acoustic resonance. Various boundary conditions could be tested to examine their response to acoustic waves.

For the simulation work, it was necessary to develop a suitable grid that modeled as accurately as possible the actual geometry and acoustic conditions of the experimental setup. A sub-scale grid could be used to develop the appropriate grid spacing required to resolve the correct temperature across a diffusion flame. White noise forcing would be provided to both the experimental setup and the simulation geometry. Then, a spectral analysis could be used to compare the results and suggest modifications to the grid geometry and boundary conditions. Once the grid was generated, a baseline steady-state non-reacting flow case could be simulated using gaseous H2-O2 co-flows. From this steady state simulation, time dependent simulations would be run with various forcing frequencies and amplitudes. The frequency and amplitude responses to flame-acoustic interaction would be compared to assess the capability of Loci-CHEM.

Following the cold flow simulations, a reacting 6-species, 8-reaction H2-O2 chemistry model could be used and a reacting flow baseline simulation would be established. Acoustic forcing would then be applied to the reacting flow steady state to provide an assessment of Loci-CHEM's handling of the aforementioned flame-acoustic interactions. Similarities and differences between the simulation results and experimental data would be examined at both low-frequency and high-frequency conditions.

1.3 Review of Other Work

1.3.1 Combustion Instability

There has been a significant amount of work done in the field of combustion instability. A very brief summary of some of the highlights of combustion instability research will be presented, with emphasis on combustion instability problems relating to liquid rocket engines.

One of the important works in the field of combustion instability was the development of the Rayleigh criterion (Rayleigh 1945). He observed that in a system involving both heat release and acoustic waves, a cumulative damping or amplification effect could occur depending on the phase of the heat release in relation to the acoustic vibrations. This can also be described by saying that when the pressure fluctuation p' and the heat release fluctuation q' are in phase with each other the total acoustic energy of the system will increase. Later, Putnam and Dennis (1953) derived a mathematical form of Rayleigh's observation. Culick (1987) then expanded upon this early mathematical definition, creating a more explicit expression relating p' and q' to the change in energy of the system. Work by Pariel and Martin (1969) utilized Rayleigh's criterion to show how the location of the velocity node of the acoustic waves could affect combustion instability.

Later work such that by Barerre and Williams (1969) examined different types of combustion instabilities and developed three categories of general instabilities, intrinsic instabilities, system instabilities, and chamber instabilities. The chamber instabilities category was further broken down into acoustic instabilities, shock instabilities, and fluid-dynamic instabilities. Candel (1992) reviewed some of the

hydrodynamic effects that could couple together pressure and heat release and lead to the development of combustion instabilities. Williams (1985) provided a wealth of detail on various aspects of combustion and combustion instabilities, including those found in liquid rocket engines

1.3.2 Instabilities in Liquid Rocket Engines

A good review of the history of instability in liquid rocket propulsion systems can be found in the works by Culick and Yang [1995] and Hulka and Hutt [1994]. An important parameter in liquid rocket combustion instability is that of time delay, and was discussed by Summerfield (1951). He also suggested that self-igniting propellants are less inclined to low frequency instabilities than non-self igniting propellants. The idea of the time delay between propellant entering the combustion chamber and the accompanying heat release is generally associated with low-frequency, 'chugging' instabilities. Work by Crocco and Cheng (1953, 1956) also looked at a time lag and examined higher frequency, longitudinal instabilities. Later on, experimental validation of these ideas was demonstrated [Crocco et al. 1960].

Experimental visualization of high frequency 'screaming' instabilities in liquid rocket engines were conducted by Male, Kerslake, and Tischler (1954). It was seen that greatly increased heat transfer to the walls occurred during periods of instability, and that this heat transfer was greater for transverse modes rather than longitudinal modes. Male and Kerslake (1954) conducted experiments showing that the presence of longitudinal fins could attenuate the amplitude of transverse modes, thus providing a mechanism for the control of combustion instability. They also noted that transverse modes first became dominant in the near-injector region, then

spread throughout the combustor. Baker and Steffen (1958) also studied high frequency instabilities in liquid rocket engines, looking specifically at gaseous GH2/LOX engines. They discovered that a mixture of liquid and gaseous propellant was less prone to screaming instabilities than all-liquid propellants. Reardon (1961) performed theoretical and experimental studies of transverse modes in high frequency instabilities. Wainhainen, Parish, and Conrad (1966) looked at a variety of variables affecting high frequency instabilities in hydrogen-oxygen rocket engines, including velocity ratio, mixture ratio, injection area and recess depth. They found stability limits for the various studied parameters. Reardon, Crocco, and Harrje (1964) studied the effect of velocity perturbations on transverse mode instabilities, and showed that tangential and radial fluctuations in velocity can impact spinning tangential modes, but not standing modes. Harrje and Reardon (1972) later put together a detailed compilation of both experimental and theoretical developments in liquid rocket engine combustion instability.

1.3.3 Shear Coaxial Injectors

Since this study is looking at simulation of a model shear-coaxial injector setup, it is important to look at a brief overview of work relating specifically to these injectors. Shear-coaxial injectors were developed in the United States in the early 1940s, and are the pre-dominant injector design used on most U.S. liquid rocket systems (reference needed). Early on very few high frequency instabilities were observed, likely due to the higher hydrogen temperatures used. However, at lower hydrogen temperatures, combustion instabilities began to develop. A variety of parameters can affect the stability of these injectors, including recess depth and

propellant velocity and temperature [Hulka & Hutt 1994]. Glogowski et al. (1994) studied potential instability mechanisms in shear-coaxial injectors, and performed experimental studies of model injectors. Ferraro et al. (1996) used a single full-size SSME preburner element and studied both cold flows and hot flows at realistic mass flow rates. Work by Strakey and Talley (2001) looked at the mixing characteristics of shear-coaxial injectors using gaseous/liquid fuel/oxidizer combinations. Ma et al. (2006) performed a numerical study of a density-stratified shear-coaxial injector flow field and demonstrated that density gradient plays a role in the interaction between acoustic waves and the flow field. Ghosh et al. (2006, 2007, 2008) performed extensive studies of a 2D model shear-coaxial injector with acoustic forcing, and performed a parametric analysis on factors affecting stability. He discovered that density gradient plays a dominant role in flame stability effects, and is a stronger factor than velocity ratio, momentum ratio, and fuel composition.

1.3.4 Flame-Acoustic Interactions

As mentioned before, combustion instability entails the coupling of heat release and pressure fluctuations. Simplified studies of the interaction of flames to acoustic waves can provide valuable insight to the combustion instability process. McIntosh (1991) studied pressure disturbances of different length scales interacting with conventional flames. Selerland and Karagozian (1998) performed a numerical study looking at the effect on a flame of strain oscillations of varying frequencies and amplitudes. Richecoeur et al. (2006) studied the effect of coupling between high frequency transverse oscillations on a setup of three cryogenic shear coaxial injectors. Using a high-speed camera he observed that a strong growth in flame spread was seen

when coupling occurred. Lang et al. (1987) used an acoustic driver to provide combustion instability control. Suzuki et al. (2007) studied the effect of acoustic excitation on a methane jet within a diffusion flame. They showed the behavior of the jet and the periodicity of its movement corresponds to the frequency of the acoustic forcing.

1.3.5 Loci-CHEM Applications

Since the objective of this work is validation of a numerical solver as applied to the problem of flame-acoustic interactions, it is also important to look at some applied computational works. In particular, an overview of other applications of the Loci-CHEM architecture will be discussed. At the NASA-Marshall Space Flight Center, Lin et al. (2005) performed some early validation work of Loci-CHEM, and discussed the important of the verification and validation process. They then compared simulated wall heat fluxes for a single element GH2/GO2 injector to experimental data and offered suggestions on recommended turbulence models. Coleman and Pal (2006) developed suggested a method of quantifying accuracy when validating heat fluxes calculated in Loci-CHEM. Tsohas et al. (2007, 2009) looked at modeling an H2/O2 multi-element injector and performing a parametric analysis of LOX post thickness, hydrogen inlet temperature, and fuel-oxidizer ratio. Roy et al. (2007) performed a verification study of the baseline k-w turbulence model within Loci-CHEM by comparing to results generated from the method of manufactured solutions. They found that for structured meshes, second order convergence is achieved, although that convergence drops to first order on unstructured meshes. Tucker et al. (2008) compared validation results for Loci-CHEM along with other

CFD solvers, and discussed differences in the results between the different methods. Hughson et al. (2007) applied Loci-CHEM to a different type of problem, looking at the flowfield around a lattice-grid missile tailfin. Computationally generated shadowgraph images compared favorably to experimental shadowgraph results. Hughson and Luke (2009) then later simulated the effects of unsteady flow on the same problem using both and RANS and hybrid RANS/LES method within Loci-CHEM. Veluri, Roy, and Luke (2010) performed a comprehensive verification of multiple transport models, turbulence models, and boundary conditions by comparing against results from the method of manufactured solutions.

2. Experimental Setup

2.1 Overview of Setup

This work is based on experiments conducted using a model shear coaxial injector rig. In order to study flame-acoustic interactions in the near-injector region, a 2-D shear-coaxial injector was built, with an acoustic loudspeaker that could be mounted to either side to provide acoustic forcing. A signal generator connected through an amplifier to the speaker was used to provide single frequency forcing, and LabVIEW was used to generate white noise forcing.

For a liquid rocket engine, shear coaxial injectors typically will provide liquid oxygen (LOX) as the oxidizer, surrounded by a co-flow of gaseous hydrogen. As the oxygen is introduced into the combustion chamber it atomizes, and a turbulent diffusion flame develops along the shear layer between the gaseous oxygen and gaseous hydrogen. Since most of the heat release occurs in this diffusion region where just gaseous reactants are present, a simplified setup can be used to model this, as shown in Fig 2.1. Although the experimental setup ignores some of the complicated physics involved with the atomization and mixing, it allows for focus on the flame-acoustic interactions that are the focus of this validation study.

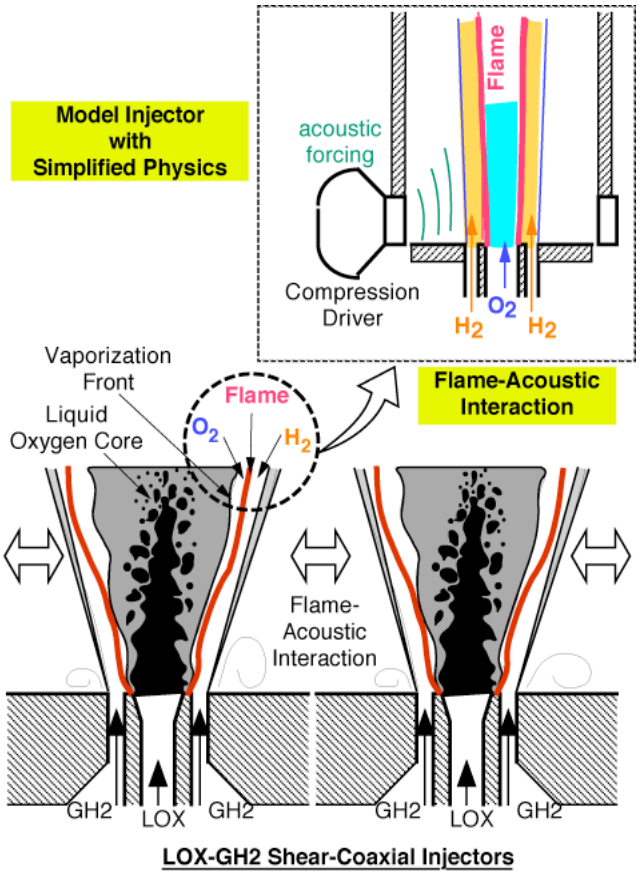

Figure 2.1: Schematic showing region of real injector field being modeled by experimental setup

Oxidizer is provided to the center jet, and two co-flows of fuel are provided to the outer jets. In this work, velocity was kept constant at 6 m/s for the center oxidizer jet, and 18 m/s for the co-flow jets. Both cold flow and reacting flow experiments were examined, with helium/air and hydrogen/oxygen being used as the fuel and oxidizer, respectively.

2.2 Combustor Hardware

2.2.1 Combustor Geometry

The model injector rig featured a rectangular combustion chamber measuring 15" x 3.5" x .375", as shown in Fig. 2.2. There was an additional height added along

the front and back due the increased height of the quartz glass windows used for visualization purposes, as the picture shows in Fig. 2.3. This brought the height along the front and back walls to 24", which proved to be an important consideration when creating the computational grid geometry. The top of the combustor chamber vents to atmosphere, although an exhaust vent located slightly above the setup provides a slight pressure gradient at the exit. A 1" x .125" slit in the side wall led to the speaker mounting.

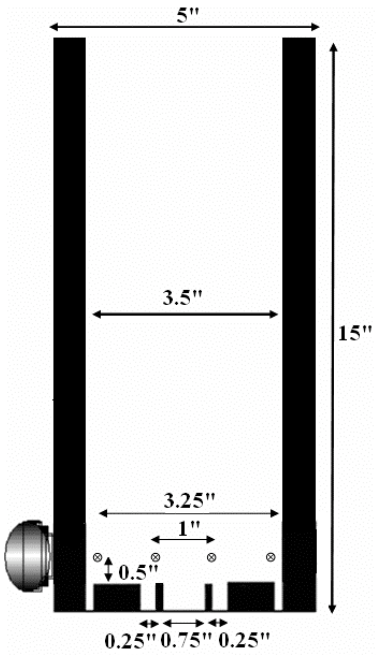

Figure 2.2: Overview of Combustor Geometry

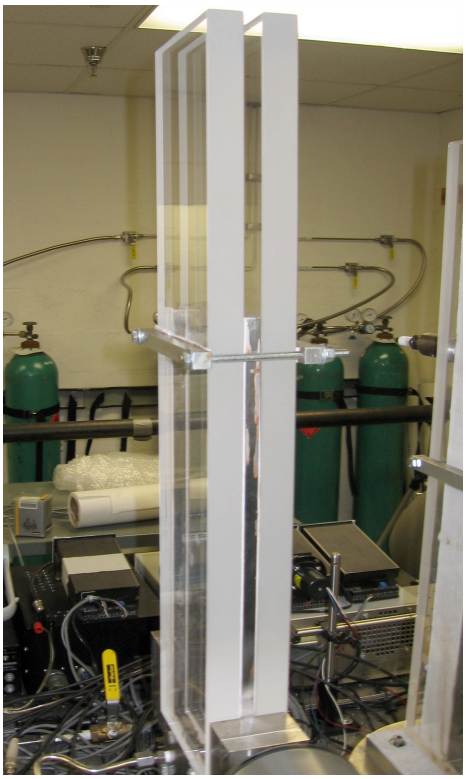

Figure 2.3: Picture of combustor with quartz glass windows

The center injection jet opening is .75” in width, and the co-flow injectors are both .25” in width. The lip thickness between them is .125”. Two .125” slits were also present next to each wall for air injection, which was used to assist in ignition, although these slits were not duplicated in the simulation. With the exception of the quartz glass viewing windows, the rest of the assembly was made of stainless steel.

2.2.2 Inlet and Feed Systems

Fig. 2.4 shows a technical drawing detailing the inlet system connecting the injector openings to the fuel and oxidizer feed lines. Fig. 2.5 shows a cutaway picture highlighting the honeycomb flow straighteners that were placed in the fuel and oxidizer posts. For simulation purposes, the computational grid was designed to simulate the post section of the inlet beginning from the exit of the flow straighteners.

This meant that a height of 4” was used for the oxidizer post, and a height of 1” was used for each of the fuel posts.

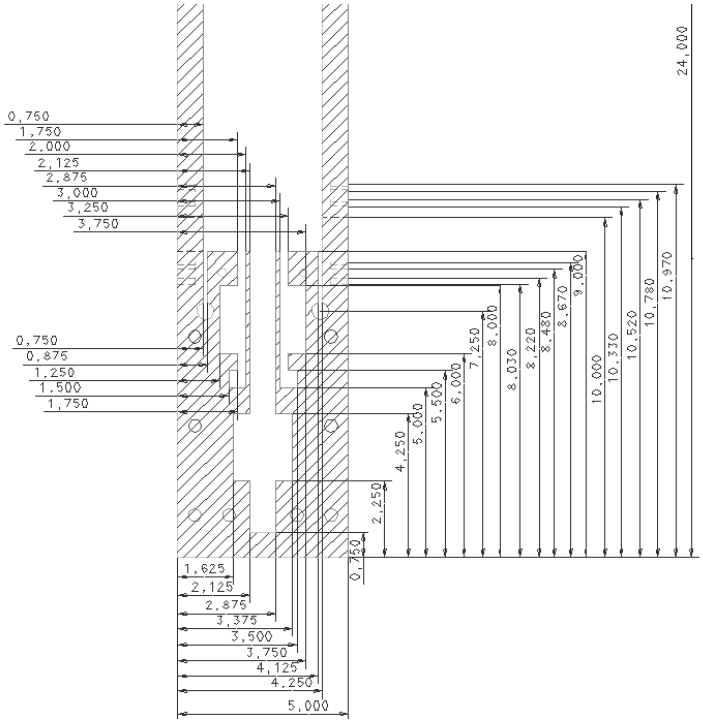

Figure 2.4: Technical drawing of combustor inlets

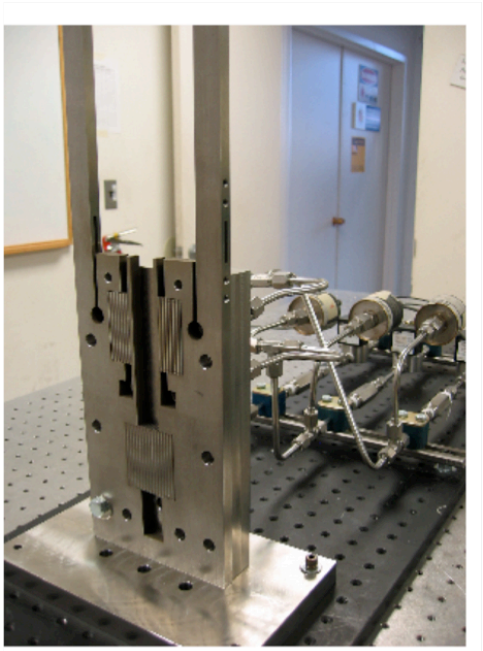

Figure 2.5: Picture showing cutaway of combustor inlets

Fig. 2.6 shows a picture of the feed lines connecting the supply tanks or house air supply to the inlet posts. One-way check valves were used to prevent back flow, and metering orifices were used to choke the flow. Serta pressure transducers were used to set the desired mass flow rates.

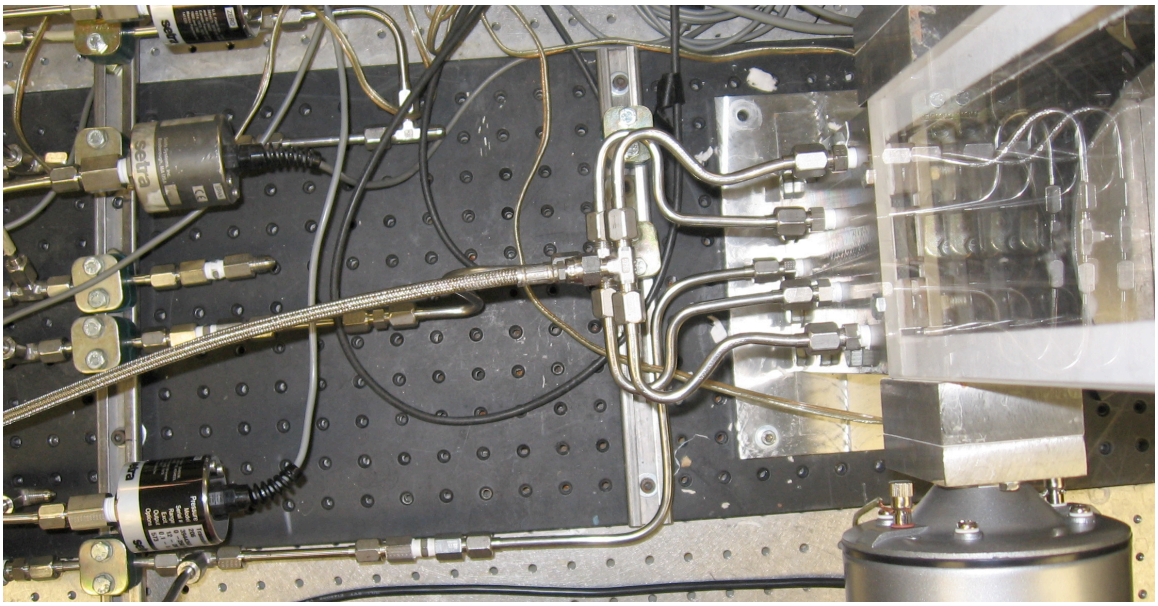

Figure 2.6: Picture of gas inlet feed lines

2.2.3 Acoustic Loudspeaker

The acoustic driver used had a normal impedance of 16 ohms and a max power rating of 100 Watts. The mounting block connecting the speaker to the wall slit smoothly transitioned from a rectangular opening to the circular speaker diaphragm, and could be mounted to either side of the setup. The acoustic driver had an optimal frequency range from 100Hz to 100,000Hz. For white noise forcing cases, LabVIEW was used to generate a white noise profile between a frequency range of 100Hz-10kHz. This was then connected to the amplifier and fed into the acoustic driver.

2.3 Diagnostics and Measurements

2.3.1 Schlieren Visualization

For the cold flow experiments, a standard Z configuration Schlieren setup was used, as shown in Figure 2.7. Two 6" diameter spherical mirrors with a focal length of 60" were used, and an arc-lamp point source was used as the light source. A 12-bit DiCam Pro ICCD camera was used to capture the images with exposure times as low as 10 μs. For the phase-locked images, synchronized signals from the wave generator controlling the speaker were fed into an IDT Laser Timing Control Board, and along with ProVision II software, triggered the camera with the appropriate phasing.

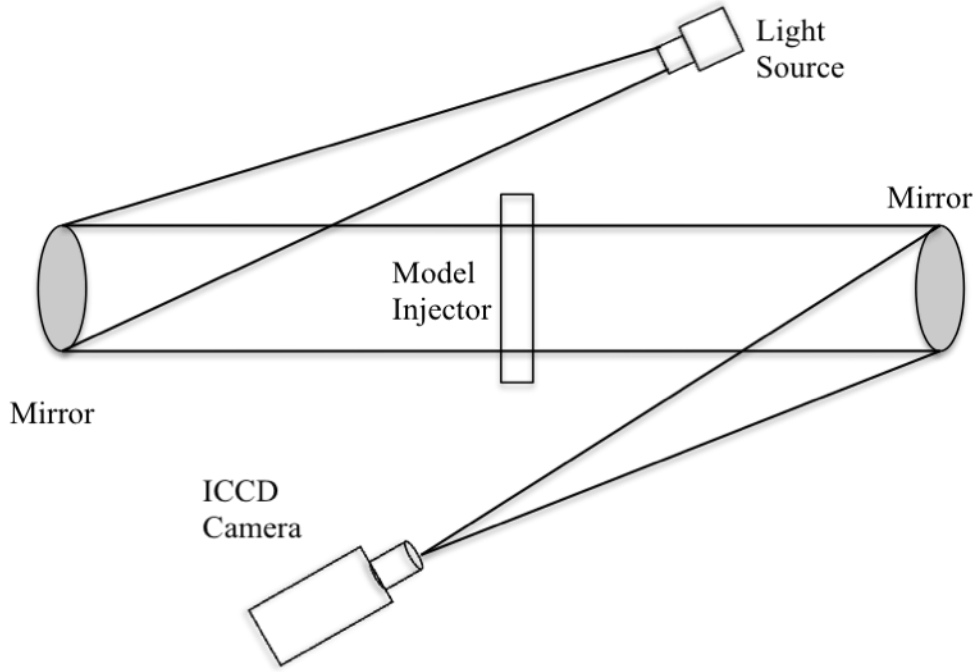

Figure 2.7: Schematic view of Z-configuration Schlieren setup

2.3.2 Phase Locked Chemi-Luminescence

To obtain imaging of the flame for the reacting flow experiments, measurements were made of the chemiluminescent radiation from the free OH* radical. Since this radical occurs almost exclusively in the reaction zone, it provides a good indication of the location of the flame and where heat release is occurring at any given instant. Phase-locked Chemi-luminescence images obtained by Ghosh [2008] were used for comparison with the reacting flow simulations.

2.3.3 Pressure Measurements

In order to take pressure measurements, one of the quartz glass windows were replaced with a stainless steel plate with four pressure tap locations, as shown in Fig. 2.8. For the reacting flows, a water-cooled adapter was used in conjunction with Kistler 211B5 pressure transducers. Output from the sensors was passed into a Kistler 5134A Piezotron coupler and from there was fed into a National Instruments Digital Acquisition Card that interfaced with a LabVIEW monitoring program. A 10kHz low-pass filter was applied via the coupler, and a gain of 100 was added. Data was sampled at a rate of 20kHz, and saved into data files through LabVIEW for later processing. For cases involving white noise forcing, a Matlab script was used to perform a FFT on the data, providing plots of the spectral amplitude in frequency space.

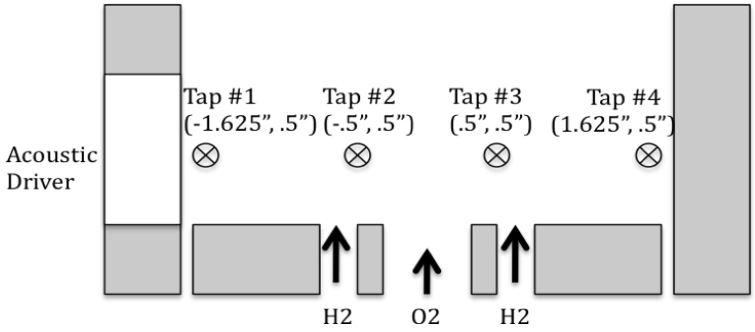

Figure 2.8: Pressure sensor locations

2.4 Previous Work

A majority of the validation data being used in this work was generated during previous work by Ghosh [2007,2008]. As part of that work, both cold flow He-Air and reacting GH2-GO2 experiments were conducted, as well as broadband forcing of the chamber under both no-flow and He-Air flow conditions. The original goal of these studies was to identify important factors relating to the onset of instability in diffusion flames with transverse forcing. The main conclusion reached was that density gradient plays a dominant role in affecting flame stability, and that Baroclinic vorticity, and torque generated by the cross product of the density and pressure gradients, may be responsible for this effect.

2.4.1 He-Air Experiments

Cold flow He-Air experiments were conducted to examine the effect of acoustic forcing on a density and velocity stratified flow field under the simplified condition of no heat release. Forcing was provided at a range of frequencies, although only those most relevant to the current work will be discussed here. For all cases looked at here, velocities were fixed at 6 and 18 m/s for air and helium respectively.

Figure 2.9 shows the baseline images obtained for the He-Air flow with no acoustic forcing present. Figure 2.10 shows the schlieren images for He-Air flow with acoustic forcing at 400Hz and 40vpp. At this frequency, symmetric flow-acoustic interactions are seen on both sides, despite acoustic forcing from only one side. This suggests that a longitudinal mode of the chamber is being excited at that frequency, resulting in the symmetric behavior.

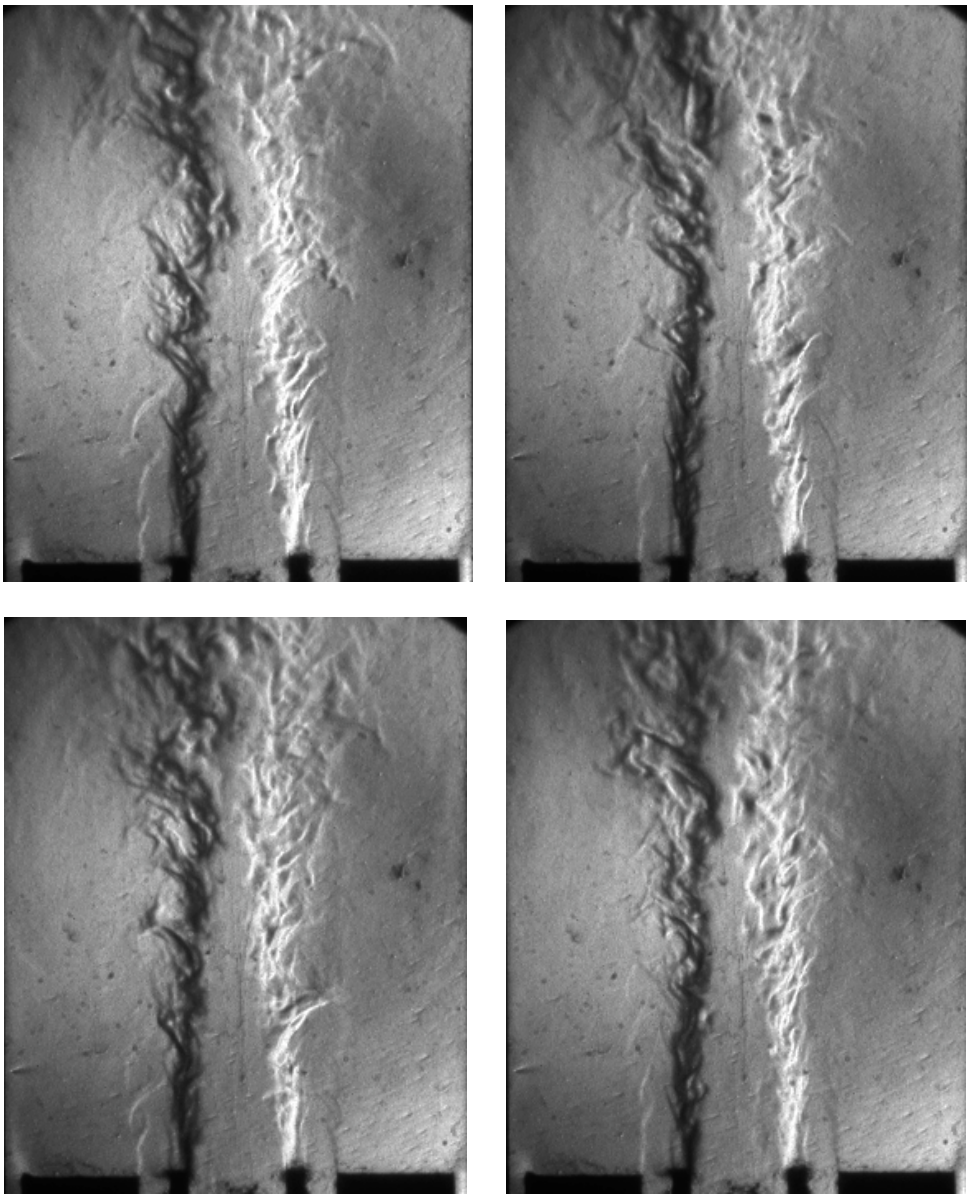

Figure 2.9: Baseline Schlieren images for He/Air/He at 18/6/18 m/s

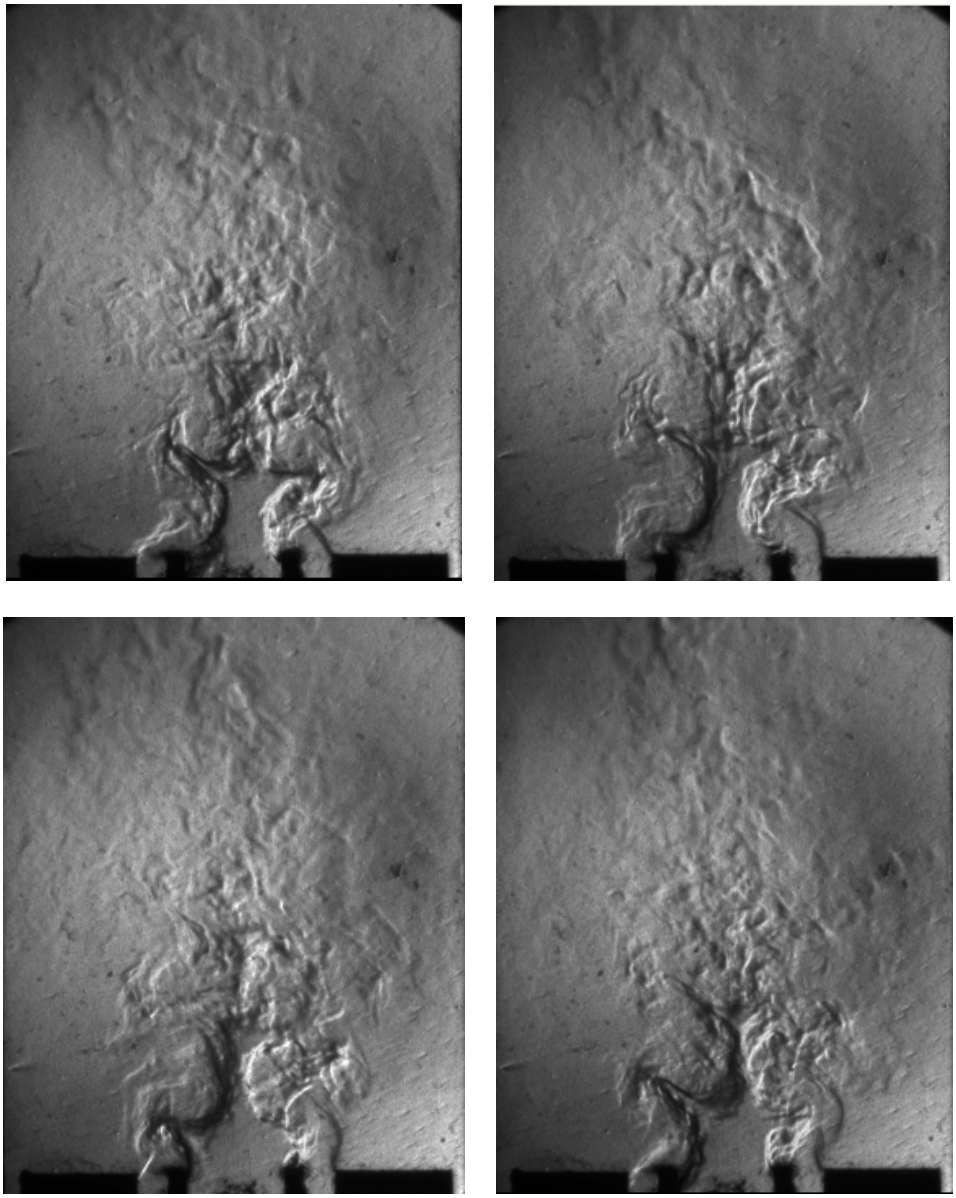

Figure 2.10: Phase-locked Schlieren Images for He/Air/He with acoustic forcing at 400Hz and 40vpp

Figure 2.11 shows the schlieren images for He-Air flow with acoustic forcing at 771Hz and 40vpp. This frequency results in a strong asymmetric interaction, with the flow bending towards the direction of forcing. Additionally, Figure 2.12 shows

the result of ramping the amplitude of the forcing from 20vpp to 50vpp while keeping the frequency constant at 771Hz.

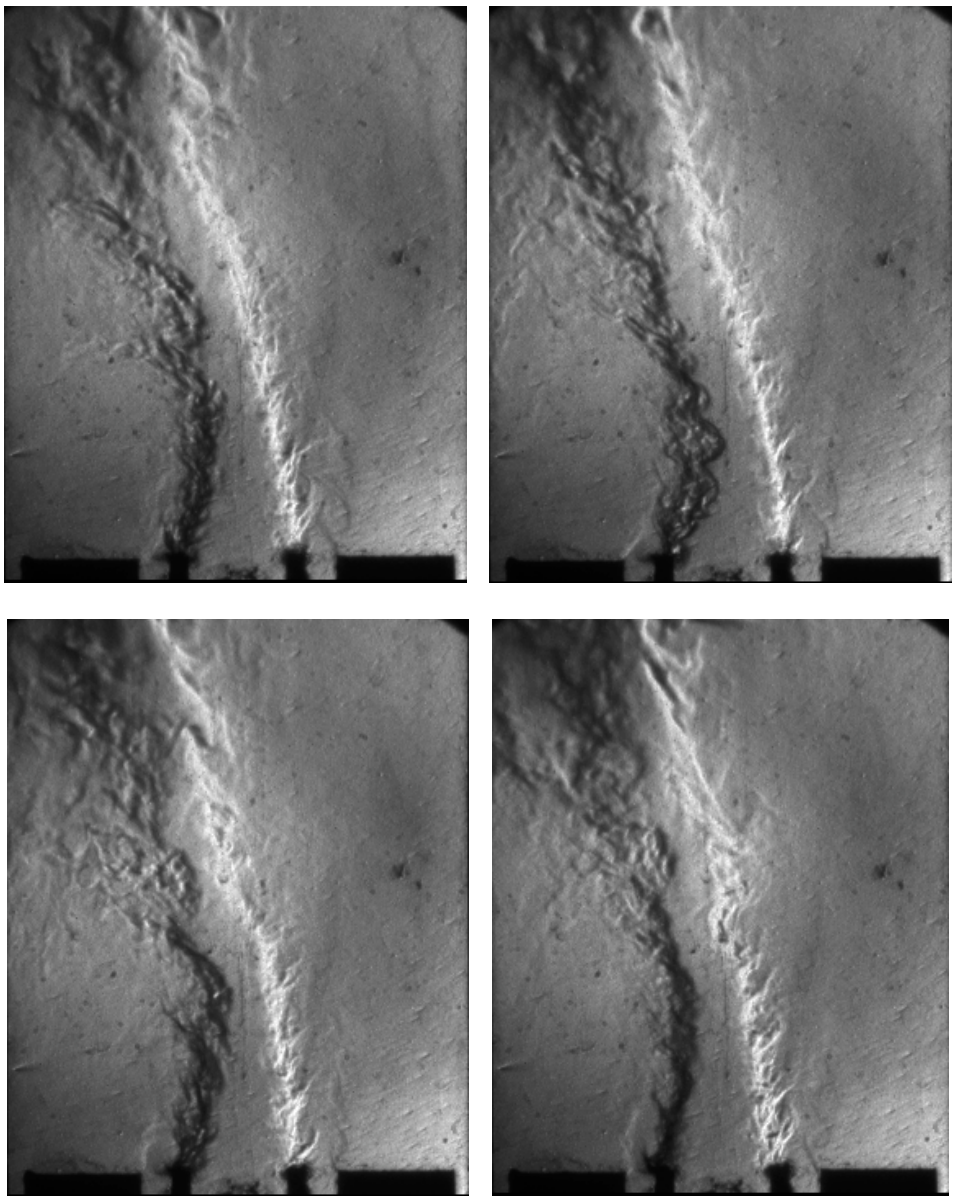

Figure 2.11: Phase-Locked Schlieren images for He/Air/He with acoustic forcing at 771Hz and 40vpp

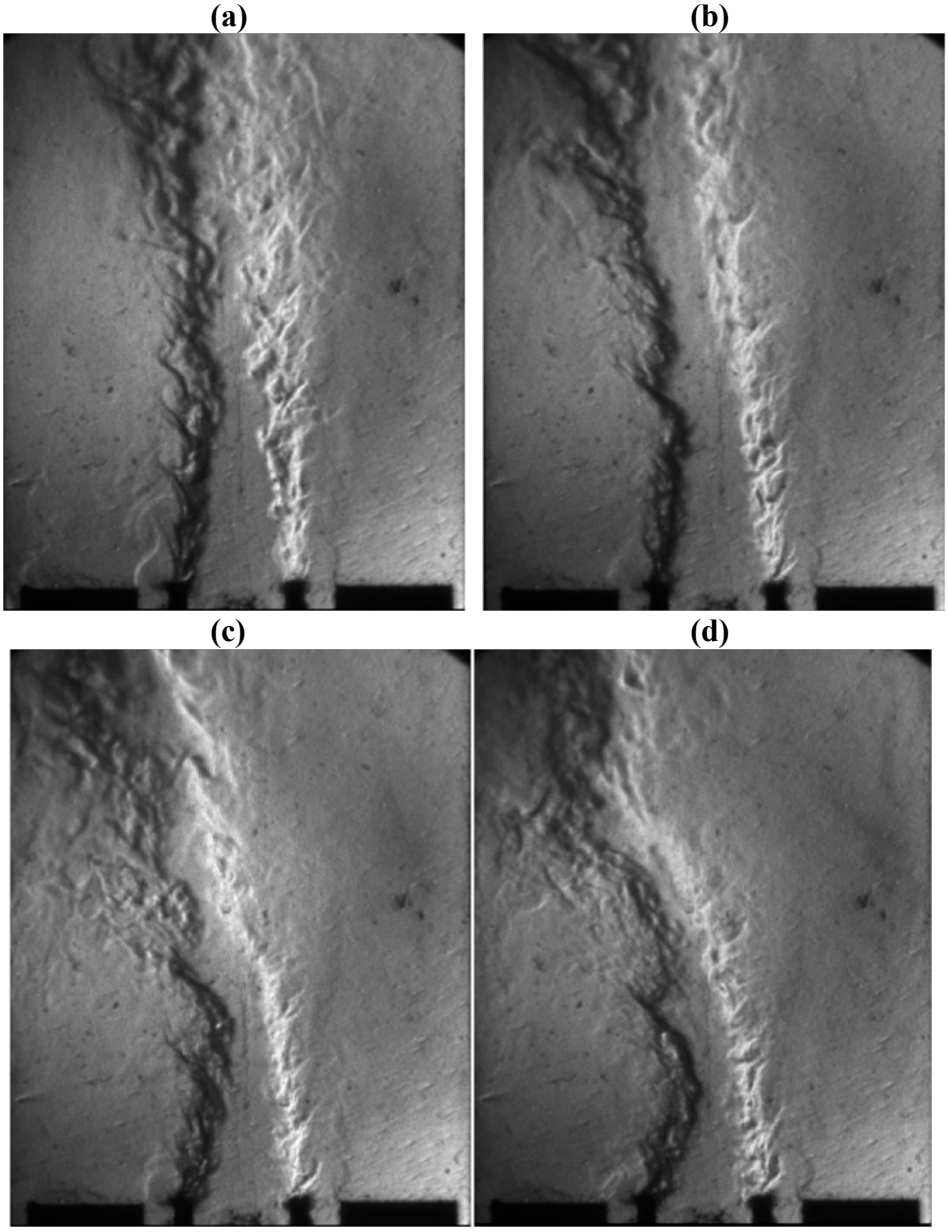

Figure 2.12: Schlieren images for He/Air/He with acoustic forcing at 771Hz, (a) 20vpp (b) 30vpp (c) 40vpp (d) 50vpp

2.4.2 Reacting Flow Experiments

The reacting experiments conducted by Ghosh also featured the same velocity ratios across the jets, but with H2 and O2 replacing the He and Air. An igniter was used to initiate combustion prior to the acoustic forcing being activated. For these experiments, OH* Chemi-luminesence and a high speed ICCD camera were used to capture flame images. Figure 2.13 shows a baseline image, with no acoustic forcing present. Figure 2.14 shows phase-locked images of the combustor being forced at 300Hz. Similar to the cold flow case, this lower frequency also showed symmetric flame behavior. However, at the higher frequency of 1150Hz, as shown in Figure 2.15, a strong asymmetric behavior is shown. In this case, the flame closest to the speaker exhibits increased instability, whereas the flame on the far side of the speaker appears to be stabilized. Assuming baroclinic vorticity as the mechanism would explain this phenomena, since the density gradient is pointing in opposite directions on either side of the center jet, and resulting torque would serve to amplify any existing disturbances in the flame near the speaker, and damp any disturbances in the flame away from the speaker.

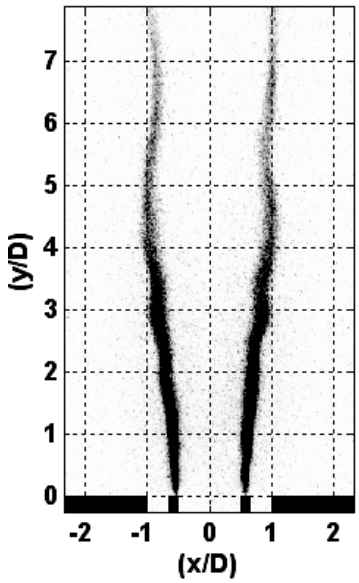

Figure 2.13: OH* Chemiluminesence showing baseline state of turbulent H2/O2/H2 flames at 18/6/18 m/s

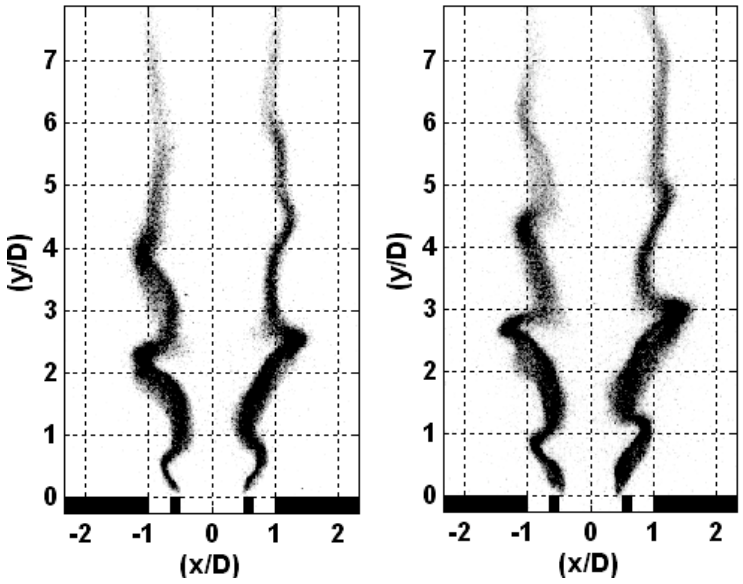

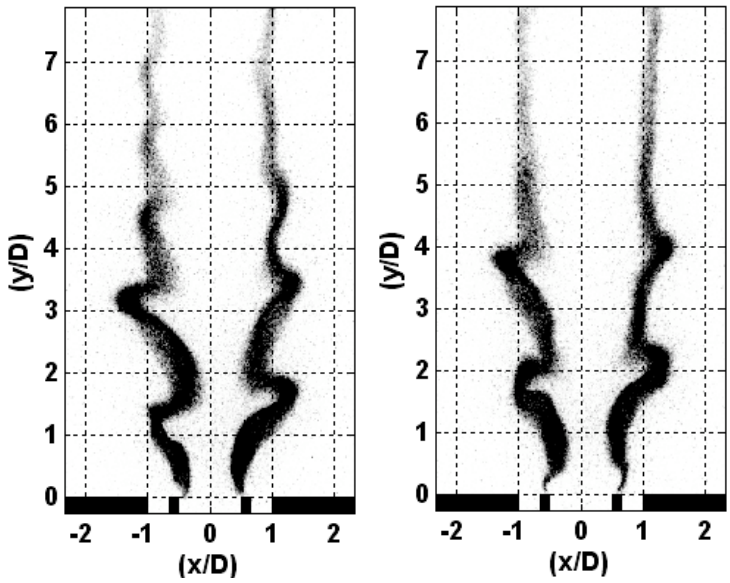

Figure 2.14: Phase-Locked OH* Chemiluminesence showing H2/O2/H2 flames forced at 300Hz

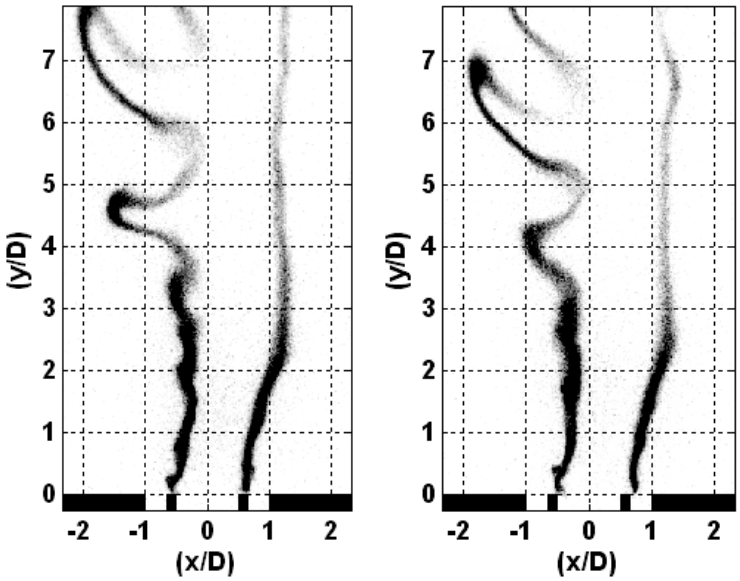

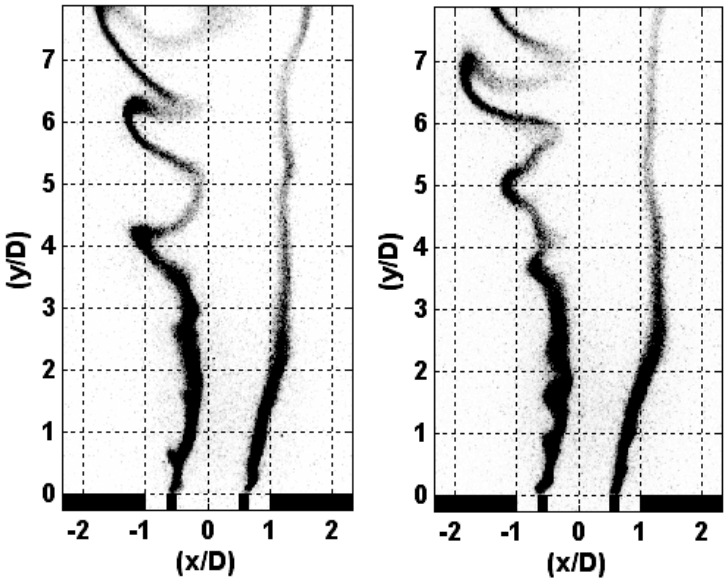

Figure 2.15: Phase-Locked OH* Chemiluminesence showing H2/O2/H2 flames forced at 1150Hz

Further studies as part of this work demonstrated that reduction of the density ratio has a stabilizing effect on the speaker-side flame under the same level of forcing. For more detail on these results, the reader is referred to the Ph.D thesis by Ghosh [2008].

3. Computational Methodology

3.1 Loci-CHEM Overview

The code being used for this work is NASA's Loci-CHEM solver, which was developed at Mississippi State University [Luke at al 2004]. Loci-CHEM is a three dimensional, finite rate chemistry viscous flow solver. It is second order in both time and space, and uses approximate Riemann solvers to solve turbulent flows and finite rate chemistry problems. Various turbulence and chemistry models can be provided, and these will be examined in more detail later in this work.

The Loci-CHEM solver uses a finite volume approach to discretize the flow equations. The overall governing equation being solved for each control volume section is of the form shown in equation 3.1, where Q is the vector of conserved state variables, F_i is the inviscid flux, F_v is the viscous flux, and $\dot{W}$ is the chemistry source term.

$$\frac{d}{dt}\int_{CV} Q dV + \int_{CV} (F_i - F_v) dS = \int_{CV} \dot{W} dV \tag{3.1}$$

For a multi-species problem with N-species, the various vector quantities are given by the following equations.

$$Q^T = [\rho_1, \rho_2, ... \rho_N, \rho u, \rho e_0] \tag{3.2}$$

$$F_i^T = [\rho_1 \tilde{u} \cdot \tilde{n}, \rho_2 \tilde{u} \cdot \tilde{n}, ... \rho_N \tilde{u} \cdot \tilde{n}, (\rho \tilde{u} \tilde{u} + p\tilde{\tilde{I}}) \cdot \tilde{n}, (\rho e_0 + p)\tilde{u} \cdot \tilde{n}] \tag{3.3}$$

$$F_v^T = [-\rho_1 \tilde{V}_1 \cdot \tilde{n}, -\rho_2 \tilde{V}_2 \cdot \tilde{n}, ... - \rho_N \tilde{V}_N \cdot \tilde{n}, \tilde{\tilde{\tau}} \cdot \tilde{n}, (\tilde{u} \cdot \tilde{\tilde{\tau}} - \tilde{q} - \sum \rho_s h_s \tilde{V}_s) \cdot \tilde{n}] \tag{3.4}$$

$$\dot{W}^T = [\dot{w}_1, \dot{w}_2, ... \dot{w}_N, 0, 0] \tag{3.5}$$

The pressure term p is determined from Dalton's law and assumes that all species are thermally perfect gases as shown in equation 3.6.

$$p = \sum_{s=1}^{N} \rho_s R_s T \tag{3.6}$$

For the chemistry source terms, the reaction rate terms are described by equation 3.7.

$$\dot{w}_s = M_s \sum_{r=1}^{NR} (v''_{s,r} - v'_{s,r}) \times [k_{f,r} \prod_{l=1}^{NS} (\frac{\rho_l}{M_l})^{v'_{l,r}} - k_{b,r} \prod_{l=1}^{NS} (\frac{\rho_l}{M_l})^{v''_{l,r}}] \tag{3.7}$$

The reaction rates are found using Arrhenius curve fits generated from constants taken from the CHEMKIN database and contained within the input chemistry model.

The viscous flux terms require knowledge of the stress tensor and the heat flux vector. The stress tensor is given by equation 3.8 with the turbulent viscosity terms being provided by one of the available turbulence models. The turbulence models will be discussed in a later section.

$$\tau_{ij} = (\mu + \mu_t)(\frac{\partial u_i}{\partial x_j} + \frac{\partial u_j}{\partial x_i}) - \frac{2}{3}[(\mu + \mu_t)\nabla \cdot \tilde{u}]\delta_{ij} \tag{3.8}$$

Fourier's Law is used to relate the heat conduction and temperature gradients, and the heat flux vector is given by equation 3.9.

$$\tilde{q} = (\lambda + \mu_t c_p / \mathrm{Pr}_t)\nabla T \tag{3.9}$$

By default, Loci-CHEM uses a turbulent Prandtl number of 0.9 for all computations, and the thermal conductivity is obtained calculations involving the transport properties of the species. The transport properties can be calculated using either Sutherland's Law if the appropriate constants are specified, or can be obtained from the CHEMKIN transport database included within Loci-CHEM.

The inviscid flux terms of the governing equation (Eq. 3.3) are solved in discretized form using Roe's flux difference splitting technique. Rankine-Hugoniot relations are used to satisfy the conditions across a shock. Close to the shocks, a modified HLLE algorithm is used in place of Roe's method to provide increased robustness.

The time-stepping uses a two-equation family of algorithms developed by Beam and Warming and given by equation 3.10 [Beam and Warming 1978].

$$\nu((1+\psi)\Delta Q^{n} - \psi\Delta Q^{n-1}) = \Delta t((1-\theta)R^{n}(Q^{n}) + \theta R^{n+1}(Q^{n+1})) \qquad (3.10)$$

In this equation, θ and ψ are two variables that determine the accuracy of the algorithm. If θ=1 and ψ=0, an implicit first order backward Euler scheme is applied, and this method is commonly used in steady-state simulations. If θ=1 and ψ=.5, it becomes a second order three point backward scheme, which is recommended for time-accurate simulations.

3.2 Verification Studies

Before examining the problem of simulating flame-acoustic interactions, it was necessary to build both familiarity with the code and a confidence in its results. To achieve both of these goals, a simple verification study looking at laminar and turbulent channel flow was conducted. The first simulation conducted was that of laminar Poiseuille flow through a rectangular duct. A 100x1x1 mm rectangular duct was simulated with viscous walls, a pressure fixed outflow of P=1atm at the exit of the duct, and a fixed mass plug flow inlet condition with an effective velocity of 10 m/s. The Reynolds number was around 600 putting this flow well within the laminar

regime. Since the pressure drop across the channel due to the laminar boundary layer can be calculated analytically from equation 3.11, this provides a good exercise to both learn basics of the code and verify elementary flow properties.

$$\Delta P = \frac{8\mu LQ}{\pi r^4} \tag{3.11}$$

Figure 3.1 shows the pressure drop as a function of distance along the channel, and Figure 3.2 shows the velocity profile near the entrance and exit of the channel, which shows the expected development associated with a laminar boundary layer. It is noticed in the pressure drop profile that some time is required for the pressure drop to become linear as the boundary layer developed. However, analyzing the linear section shows very good agreement with the theoretical value. It was also seen that if a state-fixed inlet condition was used instead of a fixed-mass condition, there was the appearance of a sudden pressure jump as the code adjusted to the necessary pressure to meet the exit conditions, since the inlet conditions are now over-specified. For this reason, the fixed-mass boundary was used as the primary inlet condition for all simulations. Turbulent channel flow was also examined, although in a more qualitative fashion. For this simulation, the velocity was increased to 100 m/s, giving a Reynolds number of around 6,000. The SST turbulence model was used for this simulation, and figure 3.3 shows the different development of the velocity profiles for turbulent channel flow.

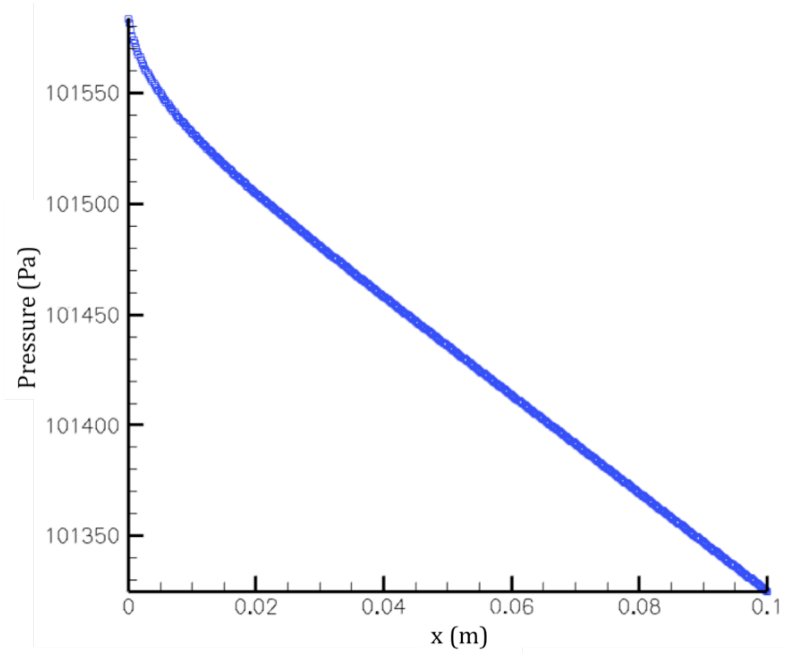

Figure 3.1: Poiseuille flow pressure drop as function of distance

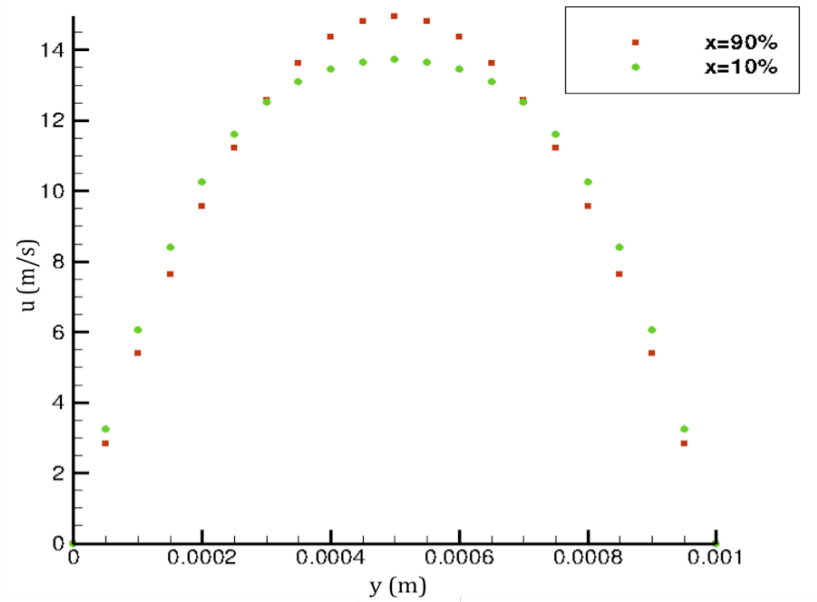

Figure 3.2 Velocity profiles in laminar poiseuille flow

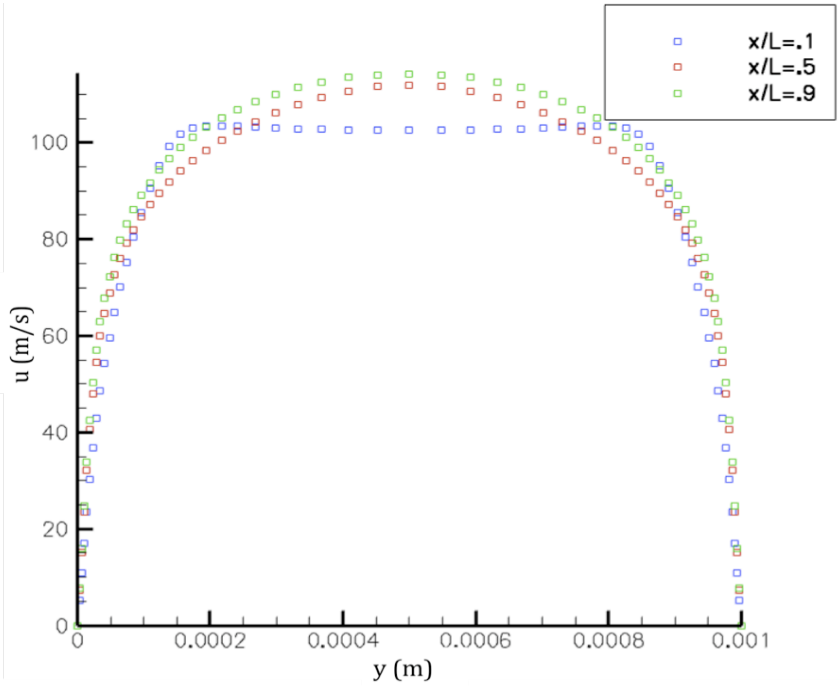

Figure 3.3 Velocity profiles in turbulent channel flow

3.3 Acoustics in Loci-CHEM

After performing these basic channel flow simulations, the next step was to examine acoustic properties within Loci-CHEM. Since acoustics are central to the main goal of this work, it was necessary to examine acoustic transmission and mode development, as well as study boundary condition interactions with acoustic waves.

3.3.1 Numerical Loudspeaker

In order to test the acoustic properties of Loci-CHEM, it was necessary to develop a method of providing controlled acoustic forcing that would simulate the same effect as the acoustic driver used in the experiments. The Tetra Extensions add-on for Loci-CHEM allows for transient boundary conditions, although only applies this to a transient fixed-mass boundary condition and a transient state-fixed inflow condition. Since previous verification studies showed that the state-fixed inflow

boundary condition had potential conflicts with over-specifying the boundary condition, it was decided to use the transient mass-flow boundary to create the numerical loudspeaker effect. This boundary condition reads in a data file provided by the user that specifies mass flow rates, total temperatures, and species fractions at a series of time steps. To provide sinusoidal forcing, the total temperature and species fraction are kept constant while the mass flow rate is given by the function shown in equation 3.12.

$$\dot{m} = B\sin(2\pi * f * t) \tag{3.12}$$

This allows for both an amplitude and frequency to be selected. This provides a constant u' variation and is designed to simulate the movement of the diaphragm of the speaker. The result of this boundary condition is that both the velocity and the density get varied in time from the changing mass flow, and from the ideal gas law the pressure is also varied since temperature is kept constant.

3.3.2 Acoustic Resonance

During experimental testing, it was determined that several of the effects seen in both the cold flow and reacting experiments at lower frequencies were likely due to the excitation of longitudinal modes of the chamber. Therefore it was necessary to verify that Loci-CHEM would generate acoustic modes when forced at the appropriate frequencies. A simple rectangular chamber was again used as a test grid, this time with dimension of .508 x .01 x .01 meters, and a grid spacing of .002 meters. Non-viscous walls and a pressure-fixed outflow were used as boundaries. The numerical loudspeaker condition was used for the inflow boundary. A time step of $5\,\mu s$ was used for all acoustic tests. A steady flow of air was used to initialize the

chamber, and once steady state was reached, the acoustic forcing was activated. Approximating the chamber as a closed tube suggested that the fundamental longitudinal frequency would occur around 167Hz. Forcing was applied at frequencies of 100Hz, 162Hz, 167Hz, 172Hz, and 220Hz to capture the effects of forcing near a resonant frequency. Pressure traces were recorded at various locations along the length of the chamber. Examining a pressure trace at x/L=.6, the ratio of the magnitude of the pressure oscillations to the steady state value were recorded for each frequency, and plotted as shown in Figure 3.4. It shows that pressure oscillations greatly increased as the resonant frequency was approached. Figure 3.5 compares the pressure traces at 167Hz and 220 Hz to illustrate the growth in amplitude near the resonant mode. These tests illustrated that Loci-CHEM could capture acoustic resonance effects and would not overly damp acoustic waves.

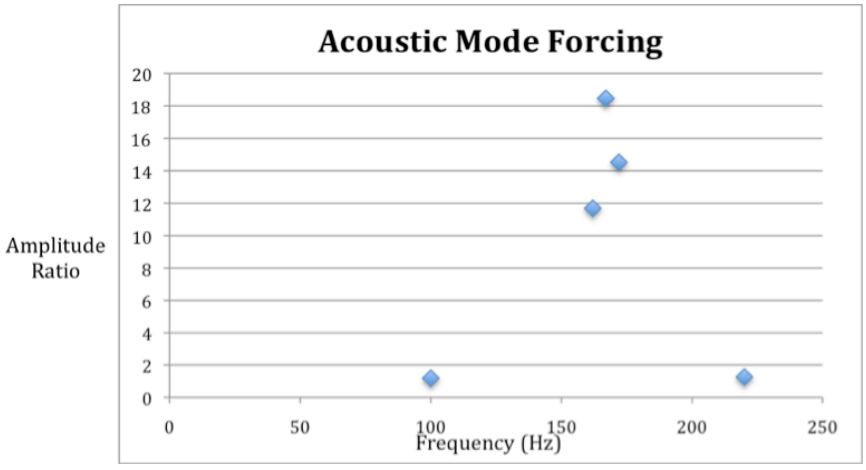

Figure 3.4: Pressure amplification ratios at various frequencies

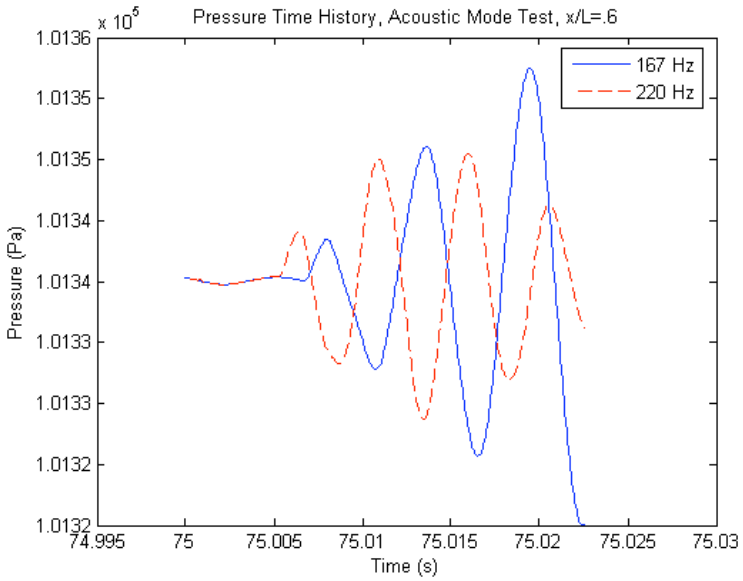

Figure 3.5: Pressure trace comparison of resonant and non-resonant frequencies

In addition to checking for acoustic resonance, it was important to consider how acoustic waves interacted with various boundary conditions, since in the acoustic resonance tests, it was observed that the pressure fixed outflow behaved as a closed boundary. Therefore a single waveform was applied to the same chamber at a fixed frequency while the opposing boundary condition was varied. Three different boundary conditions within Loci-CHEM were examined, including the Pressure-Fixed Outflow BC, the Extrapolate BC, and the Impermeable BC. Figure 3.6 shows results for all three. The first wave is the initial traveling wave, and the second occurrence is the reflected waveform. In the case of the impermeable BC, perfect reflection was achieved, with no change in phase. For the pressure fixed outflow BC, 100% reflection in magnitude was also seen although with a 180 degree change in phase. For the extrapolate BC, a 180 degree change in phase was seen, although with only 2.5% reflection in magnitude. Ideally, the exit boundary should transmit most of the energy, while only reflecting some to allow for resonance. Although the

Extrapolate BC appears to have desirable characteristics, it functions less well when applied to the actual model combustor geometry. Therefore other methods are needed to provide appropriate acoustic boundary conditions at the exit. This will be discussed more in a later section.

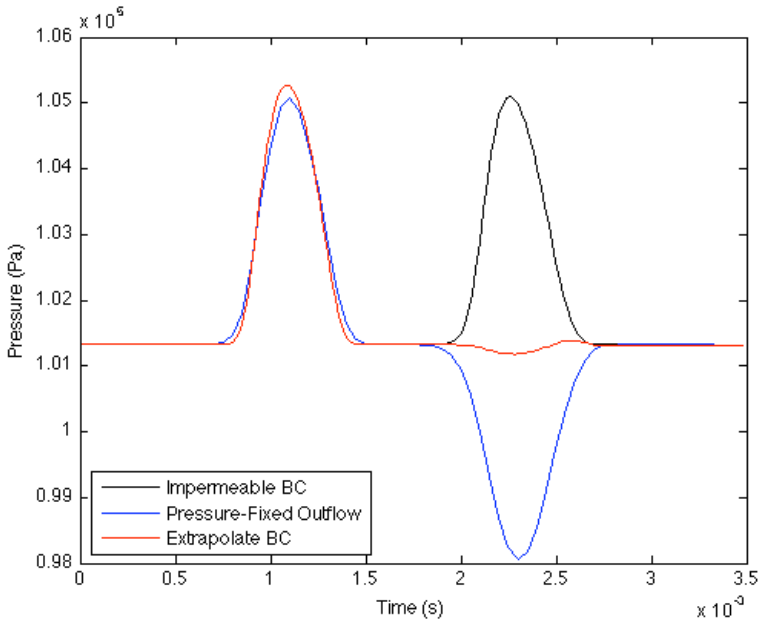

Figure 3.6: Comparison of various boundary conditions when exposed to incoming acoustic waves

3.4 Numerical Framework

Loci-CHEM allows for a large range of freedom in setting both modeling parameters as well as other numerical settings. In general, many of the numerical controls were set at the recommended values as provided in the CHEM User Guide. However, it is worth taking a more in-depth look at several of the more important parameters.

3.4.1 Turbulence Modeling

Although Loci-CHEM features a hybrid RANS/LES mode, it still requires a specified turbulence model and several models are supported within Loci-CHEM. The Spalart-Allarmas model is the only one-equation turbulence model supported by Loci-CHEM. There are two classic two-equation models. The k-ε models are commonly used in variety of engineering application for low-Reynolds number problems. However, this method can suffer from numerical stability problems under certain situations. Another common two-equation turbulence model is the k-w model developed by Wilcox. This model improves the numerical stability properties, but is found to have a very strong dependence on the value of w that is provided when applied to free shear layers. Both the original Wilcox k-w model and the updated 1998 version, which adjusts some of the dissipation terms, are supported in Loci-CHEM. Also included is the Baseline (BSL) model, which combines features of both Wilcox's k-w model with the k-ε models. Menter's Shear Stress Transport (SST) model is an updated version of the BSL model that more accurately predicts adverse pressure gradient flows [Luke et al. 2004].

A simple version of the combustor geometry was used to test the different models and compare the resulting mixing. Figure 3.7 shows H_2 mole fraction in the non-reacting flow mixing problem computed using the various turbulence models. For the purposes of this study, the Shear Stress Transport (SST) model was selected, since it displayed reasonable mixing properties as compared to experimental results. Although there is little difference between the BSL and SST results, the SST is a

more updated version of the BSL model and is known by users at NASA to be well-supported in the Loci-CHEM framework.

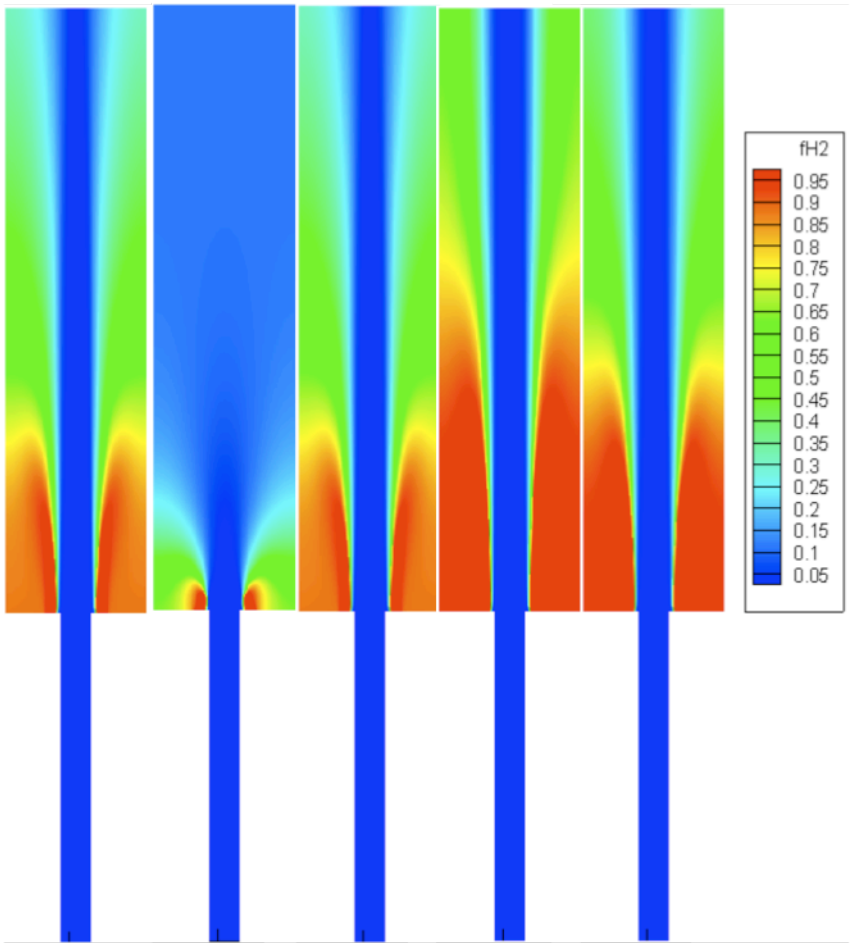

Figure 3.7: Mole fraction of H_2 in the model combustor computed using various turbulence models. (a) BSL Model, (b) Spalart-Allarmas, (c) SST Model, (d) Wilcox 98 Model, (e) KW Model

3.4.2 Chemistry Modeling

Another input to Loci-CHEM is the ability to select chemistry and reaction mechanisms. These are based on the CHEMKIN database, and several reaction models are provided as built-in options. A 1-species default air setting can be used to

simulate a standard atmospheric mixture, and this setting is used for all of the verification exercises, as well as all the baseline acoustic tests. Several H2-O2 models are available, including a non-reacting H2-O2-N2 set, a global 4-species 2-reaction H2-O2 model, and a 6-species, 8-reaction model. The global and the more detailed reaction mechanisms are shown in Tables 3.1 and 3.2, along with the values being used to compute the rate constant from the Arrhenius equation. The rate constant k is determined from a modified Arrhenius equation of the form shown in equation 3.13.

$$k_{f,r} = A(T/T_0)^n e^{-E/RT} \tag{3.13}$$

The non-reacting H2-O2-N2 model was used for all non-reacting H2-O2 simulations. Nitrogen was used as the initial ambient condition in this case. For the reacting cases, the 6 species, 28-reaction model was used since it included more intermediate species, and OH mole fraction provides a direct comparison to experimental results. Since Nitrogen was not available within this model, room temperature H2O was used as the initial ambient condition.

H2+O2 <-> 2OH
2OH + H2 <-> 2H2O

Table 3.1: Global H2-O2 Reaction Mechanism

6 species H2-O2 Reaction Mechanism	A	n	E/R (K)
H2 + M <-> 2H + M	5.5×10^{15}	-1	9059
O2 + M <-> 2O + M	7.2×10^{15}	-1	10116
H2O + M <-> OH + H + M	5.2×10^{18}	-1.5	8455
OH + M <-> O + H + M	8.5×10^{15}	-1	5586
H2O + O <-> OH + OH	5.8×10^{10}	0	51987
H2O + H <-> OH + H2	8.4×10^{10}	0	59340
O2 + H <-> OH + O	2.2×10^{11}	0	59386
H2 + O <-> OH + H	7.5×10^{10}	0	50830

Table 3.2: 6 species H2-O2 Reaction Mechanism

3.4.3 Numerical Considerations

In addition to the turbulence and chemistry models, there were many additional numerical options available within Loci-CHEM. Transport and diffusion models could be selected independent of the chemistry model, but for all simulations within this work both models were set to use the Chemkin database for their calculations. The Barth limiter was used for the reacting flows, and the Venkatakrishnan limiter was used for most verification and cold flow simulations. For the time-dependent simulations, three Gauss-Seidel iterations were used per timestep, along with two Newton iterations. For all tests involving acoustics, the simulation was run at a timestep of $5\,\mu s$, since it was found to be near the stability limit for the reacting flows, and also provided sufficient resolution of the acoustic waves. The RANS only mode was used for all acoustic only tests and verification exercises. For the cold-flow and reacting flow simulations, a steady state was achieved using the RANS only solver, and then the RANS/LES hybrid mode was activated before beginning any time-dependent simulations.

3.5 Grid Design

3.5.1 Grid Refinement Study

For the initial acoustic tests, grid spacing was selected such that acoustic waves with a frequency under 10 kHz would be fully resolved by the grid. For the cold flow mixing and the reacting flow problem, it was necessary to perform a grid refinement study to determine the minimum grid spacing required. A small-scale simulation of an oxygen-hydrogen diffusion flame was conducted at various grid spacing, and the temperature profile across the flame was examined to determine

acceptable grid spacing for a RANS/LES simulation. It was assumed that grid spacing capable of properly resolving the diffusion flame would also be sufficient in the case of the cold flow mixing problem. The test grid was half the width of the model injector, and extended a height of 6 inches. Since the combustion and mixing is dominated by shear effects, it was decided that the x-direction would have the most stringent grid spacing requirements. To minimize computational costs while still keeping reasonable cell aspect ratios, the spacing in the y- and z-directions was selected based on the x-direction spacing such that an aspect ratio of 4 was maintained. Two initial cases were studied, one with spacing of 320 microns in the x-direction, and one with spacing of 160 microns. Reducing the grid size any further proved to be very time-consuming computationally, and also resulted in difficulty achieving convergence. Figure 3.8 shows the mole fraction of OH for both cases, and qualitatively they appear almost identical. Figure 3.9 shows the mole fraction for both cases at y/H=.3 as a function of x-location. The 320 micron case closely overlaps with the more refined grid, although is just barely able to resolve the peak, suggesting it may be close to the minimum acceptable resolution. Figure 3.10 moves up to y/H=.5 and looks at the same comparison. In this case, the coarser grid shows some difference from the finer grid, but still captures the appropriate width and peak of the flame.

Ideally, 160 microns seems like an optimal grid spacing, but this proved to be infeasible due to limits on available computational power. The memory required for a grid of that size exceeded the memory available on the computer being used to run these simulations. As a compromise, a grid was designed that featured an

intermediate spacing of 260 microns within the diffusion zone so that the flame and mixing could be properly resolved. Outside this area, a spacing of 400 microns was used.

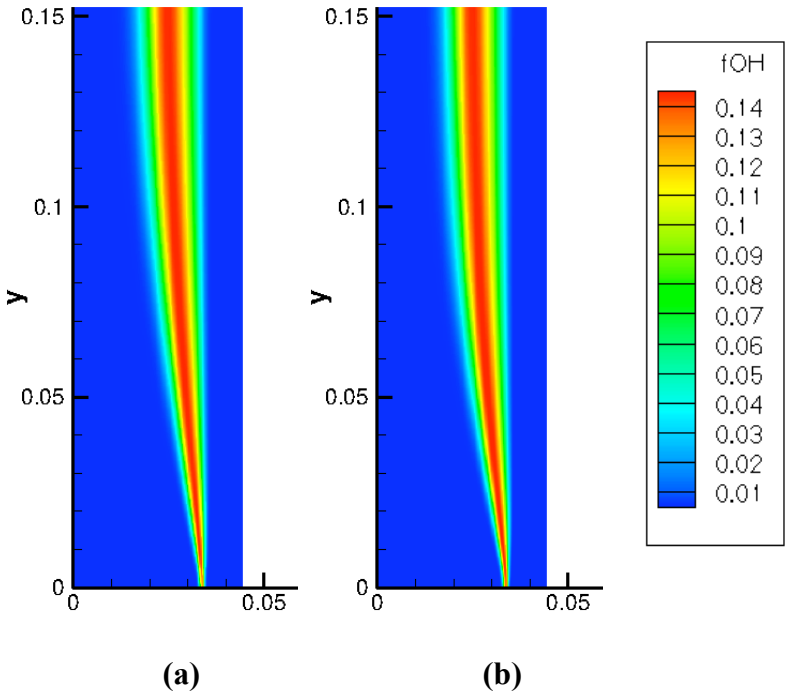

Figure 3.8: OH mole fraction comparison, (a) grid spacing in diffusion zone is 320 micron, (b) grid spacing in diffusion zone is 160 micron.

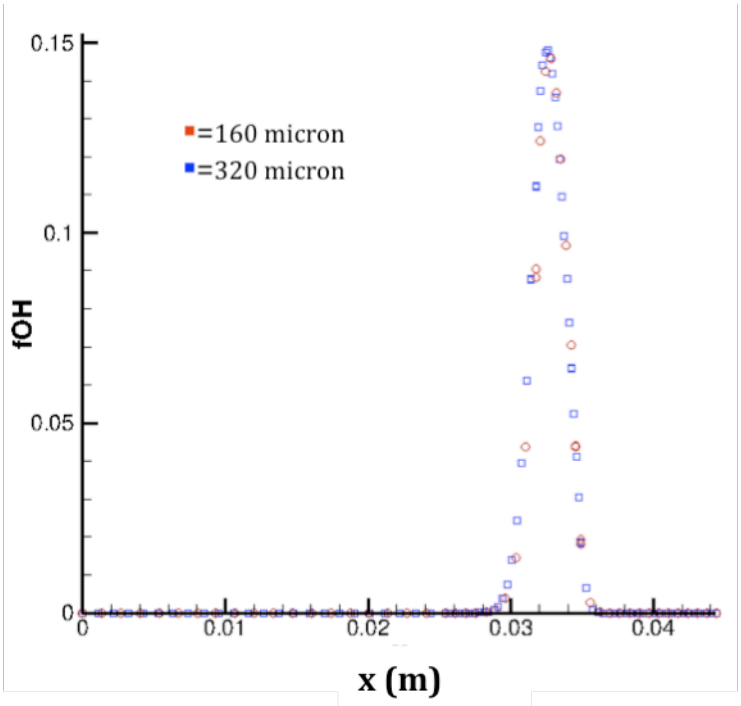

Figure 3.9: OH mole fraction at y/H=.3,

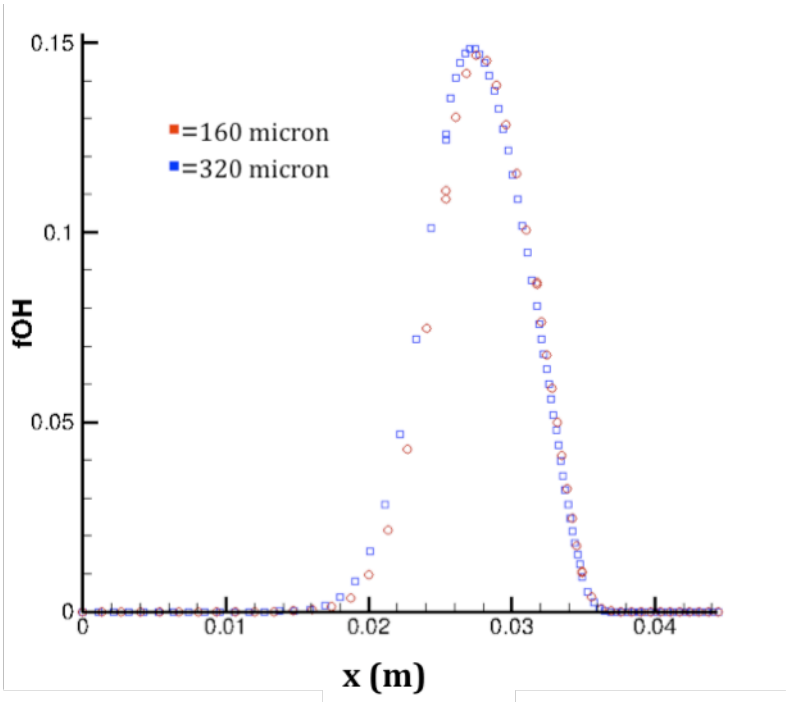

Figure 3.10: OH mole fraction at y/H=.5

3.5.2 Grid Geometry

The injector grid is closely based on the experiment setup, although several iterations were required to design a more accurate representation. Similar to the experimental setup, flow is introduced through the hydrogen and oxygen posts. For the simulation, the bottom boundary is assumed to begin at the exit of the honeycomb section in the experimental setup. This gives a length of 1" for the hydrogen posts and 4" for the oxygen posts. Fixed mass inflow boundaries were provided for the O2 and H2 inflow, and selected such that velocity was 6 and 18 m/s respectively. The plenum area that was simulated had dimensions of 5'x10'x5'. The numerical loudspeaker was initially modeled as a 1" high section of the side wall, starting from the injection plane, although these were later modified after initial white noise testing.

3.5.3 White Noise Forcing

In order to check the acoustic properties of the combustor grid, white noise forcing was applied to obtain a power spectrum that illustrated the resonant frequencies of the chamber and could be compared to experimental data. Experimentally, white noise was provided at a frequency range of 100-5000Hz, with a 5000Hz low pass filter applied to the output. The same profile was also used in the simulations. Since LabVIEW output a profile in terms of power to the speaker, this needed to be converted to mass flow for the simulation. To achieve this, the power profile was considered to be an acoustic power of the form:

$$P = v^2 \rho c A \tag{3.14}$$

The area, density of the medium at the boundary, and the speed of sound at the boundary were all known, and so the equation could be solved for velocity. Since the

power could have either sign, the absolute value of power was used, and the appropriate sign added after taking the square root. Once velocity was obtained, it was possible to calculate mass flow, and apply this profile as the numerical loudspeaker boundary condition.

This white noise profile was applied to the combustor with air only, and with probe data in the simulation being recorded at the same location as the pressure sensors in the experimental setup. Probe data was taken at a frequency of 20kHz, the same as the experiment. The same Matlab FFT script used to post-process the experimental results was used to post-process the simulation results, although frequency resolution was decreased for the simulation results since the total amount of data was limited to runtime and computer constraints. Although probe data was taken from both the speaker-side and far-side pressure transducer locations, white noise comparison is done using the far-side location data, since it is further removed from the direct effects of the speaker.

Figure 3.11 compares experimental and computational normalized spectral amplitudes. There is not a lot of agreement between the two, suggesting that the combustor grid is not properly modeling the acoustics. Since the previous boundary condition tests showed that the boundaries did not show ideal acoustic behavior, it was decided to add a simulated plenum area to increase acoustic accuracy at the exit of the region of interest. Adding a plenum provided proper modeling of the gap in the experimental setup between the front and back quartz glass and the stainless steel side walls. The plenum allowed for proper inflow-outflow to occur at this exit of the combustor, since none of the exit boundary conditions allowed for the possibility of

inflow due to a pressure gradient generated by the difference between the jet speed and the ambient air. Figure 3.12 compares the experimental to simulated spectra using the new grid with a plenum. While there is significant improvement there is still a noticeable discrepancy in the higher frequency region. This is presumably due to errors with the grid in capturing the transverse modal frequencies. To correct for this, the speaker attachment slits were added to either side. Since the speaker in the experimental setup can be attached to either side, there is a .75”x1”x.125” slit on either side, which can be either sealed at the end, or open to the speaker attachment. After adding these slits, a distinct shift in the frequency believed to be associated with the transverse mode was seen in the computational white noise forcing, as shown in Figure 3.13. This led to another improvement in agreement between simulation and experimental white noise results. The significant discrepancies at very low frequencies may be due to the very small amount of data generated by the simulation since computational time was very limited. For all three cases, less than .5 seconds of data was generated, but this is sufficient to begin to show the general shape of the spectral amplitude plot and suggest areas of reasonable agreement.

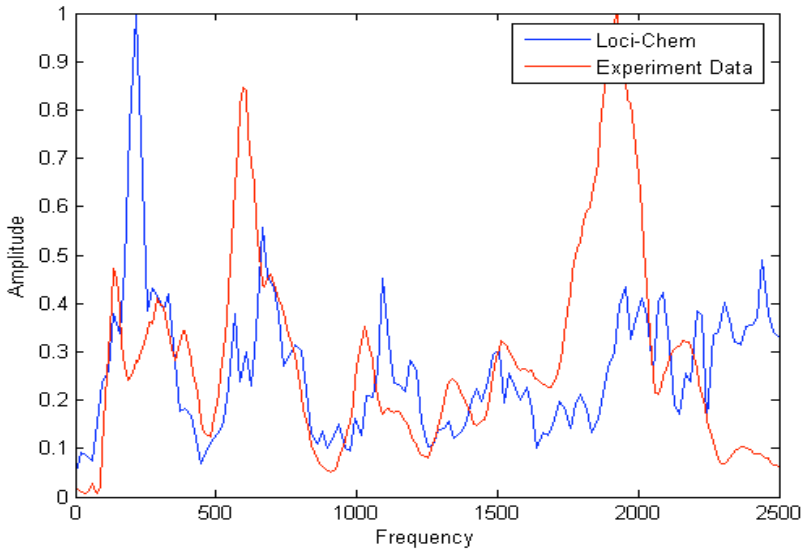

Figure 3.11: White noise comparison without plenum or speaker slits

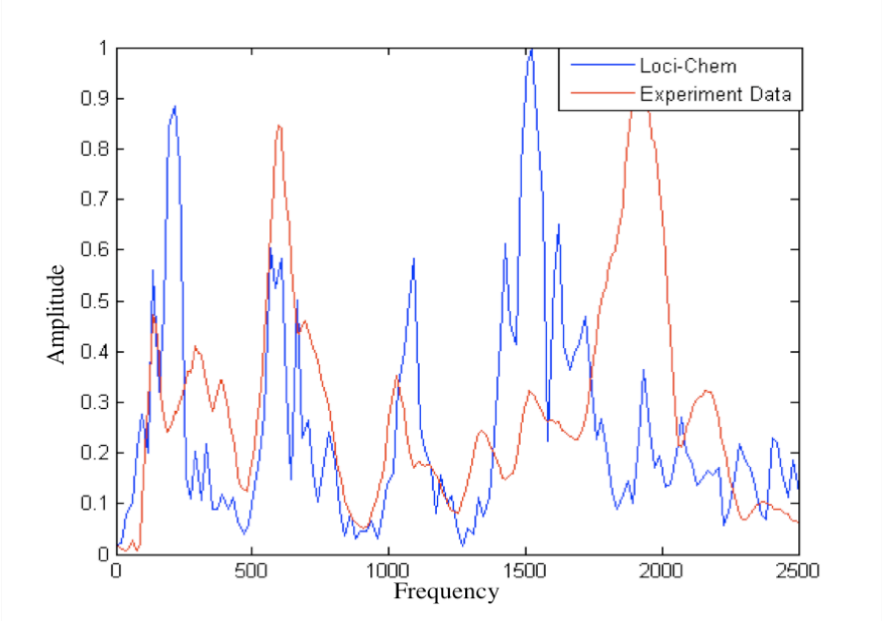

Figure 3.12: White noise comparison with plenum and without speaker slits

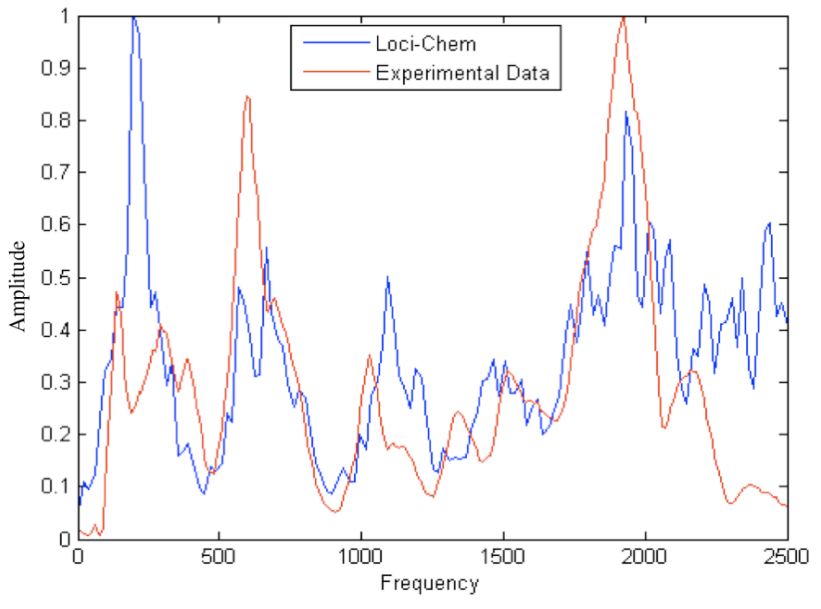

Figure 3.13: White noise comparison with plenum and speaker slits

To minimize the additional computational cost, the plenum area was designed as an unstructured grid with increased point density near the combustor exit, and low point density farther away from it. The boundaries of the plenum were set as a state fixed Farfield condition.

3.5.4 Boundary Conditions

When selecting the proper boundary conditions, it was necessary to work within the framework provided by Loci-CHEM. The solver offers many different options for boundary conditions, although not all are suitable for the setup being simulated in this work . For the inflow conditions at the entrance to the fuel and oxidizer posts, a fixed mass boundary condition was used. Total temperature was fixed at 300K, and mass flow values were selected to achieve the appropriate velocities for both fuel and oxidizer based on their respective densities and inlet areas. The walls of the combustor were all modeled as adiabatic no-slip walls. The

adiabatic condition is not exact, since there is some heat transfer into the walls. However, since the simulations typically cover a time frame of less than a second, it is reasonable assumption since there is insufficient time for any significant heat transfer through the walls to occur. The plenum boundary conditions were the most difficult to model. As discussed previously, there were no appropriate boundary conditions to model the exact exit of the combustor or the opening of the side walls that would allow for proper inflow-outflow or proper transmission/reflection of acoustic waves. Since no other boundary conditions were available, it was decided to use a plenum to move the influence of the boundary conditions as far as reasonably possible from the combustor, and instead model the immediate surroundings as ambient conditions. The outflow boundary condition, which applies a pressure fixed state to the boundary, was then moved to the top exit of the plenum, and set to a pressure of .99atm to simulate the suction effect of the exhaust vent located above the experimental setup. It was seen that applying the outflow boundary condition to the entire plenum would not work, since errors occurred if the boundary condition did not experience a net mass flow out, and along the sides some mass is pulled into the plenum area. Therefore a farfield state-fixed boundary condition was used. This specified atmospheric conditions of P=1atm, u=0, and T=300K. Using this boundary condition it was then possible to achieve convergence on the full mesh with the plenum included. As was shown in the previous section, the acoustic profile of the combustor chamber was also improved by the addition of the plenum and appropriate boundary conditions. Table 3.3 shows a complete list of the boundary conditions used and their corresponding prescribed quantities.

Boundary	BC Label	Prescribed Quantities
H_2 Inflow	fixedMass	T_0=300K, mdot=9.785e-5 kg/s
O_2 Inflow	fixedMass	T_0=300K, mdot=.001424 kg/s
Top of Plenum	Outflow	P=.99atm
Plenum Walls	Farfield	P=.99atm, u=0 m/s, T=300K
Combustor Walls	viscousWall	Adiabatic
Numerical Loudspeaker	fixedMass	transientMdot data file

Table 3.3: List of boundary conditions

3.5.4 Finalized Grid and Boundary Conditions

After performing the white noise forcing and grid resolution study, a final grid was developed to use for the cold-flow and reacting flow simulations. A total of 793,349 grid points were used to create a total of 1,312,133 computational cells, including both the structured and unstructured sections. Figure 3.14 shows an x-y plane slice of the overall grid, with appropriate boundary conditions labeled. Figure 3.15 shows a zoomed view of the grid near the exit to the combustor where the transition from structured to unstructured occurred. Figure 3.16 shows a zoomed view of the near injector field showing the increased grid density in the shear layer. Figures 3.17 and 3.18 showed a zoomed view of one of the speaker slit attachments that is modeled by this grid.

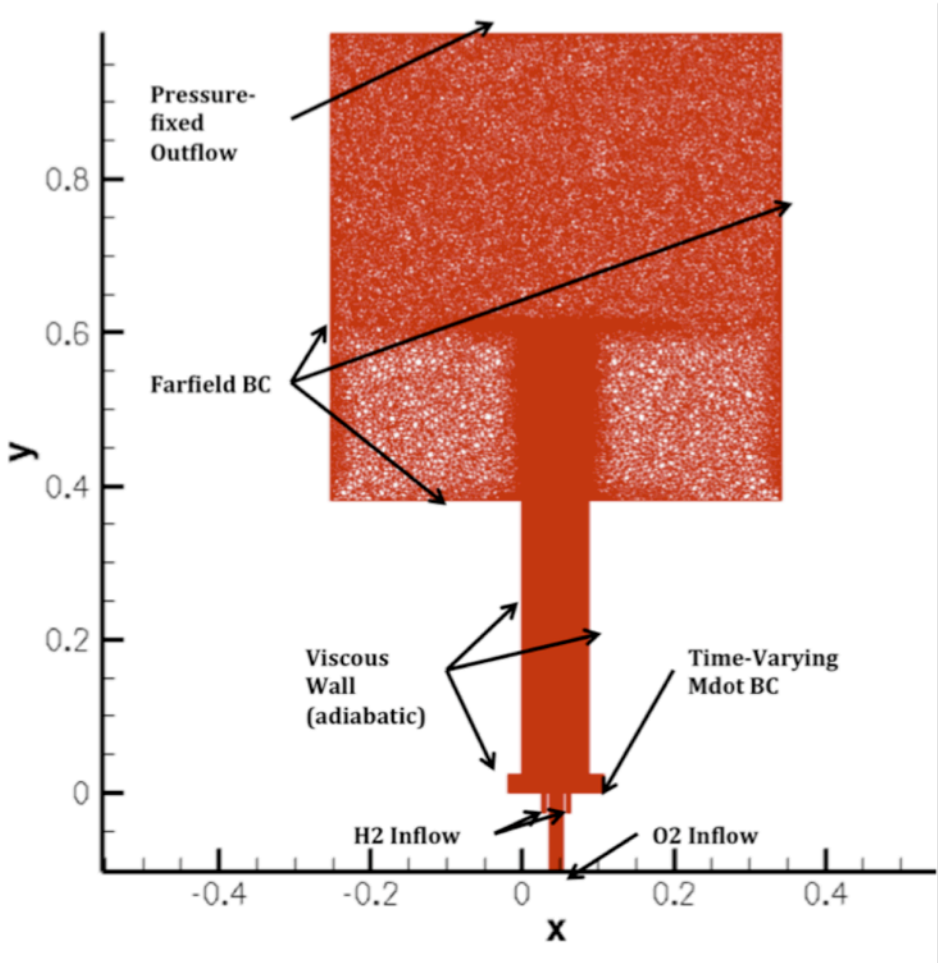

Figure 3.14: Combustor grid with labeled boundary conditions

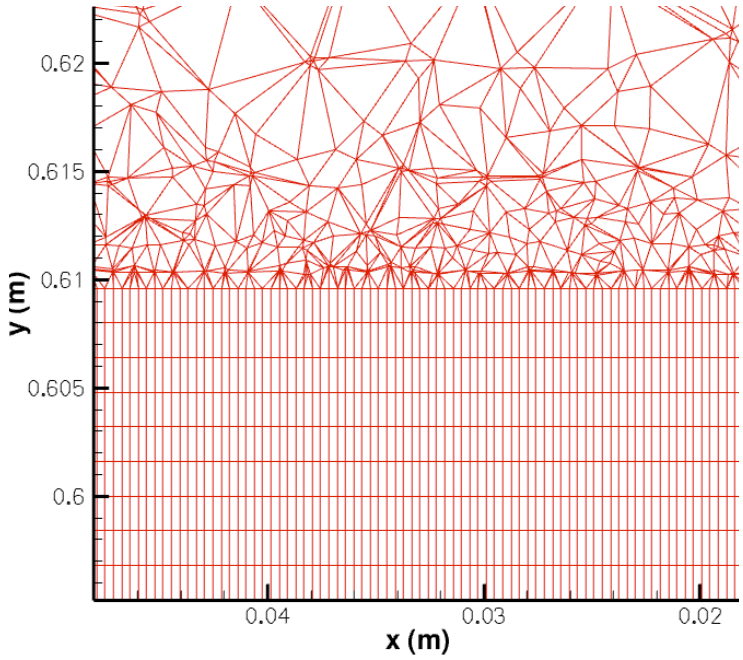

Figure 3.15: Zoomed view of combustor mesh showing combustor exit

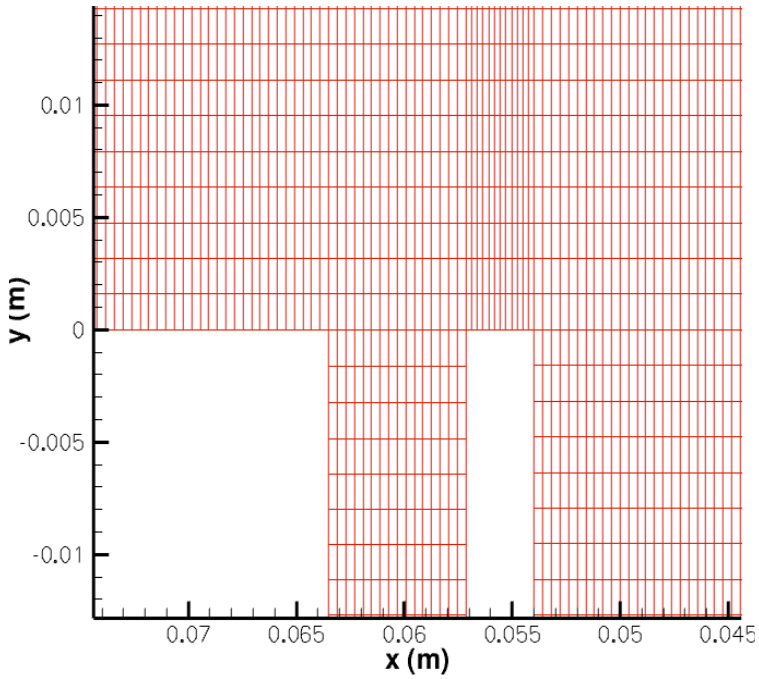

Figure 3.16: Zoomed view of combustor mesh showing inlet and shear layer region

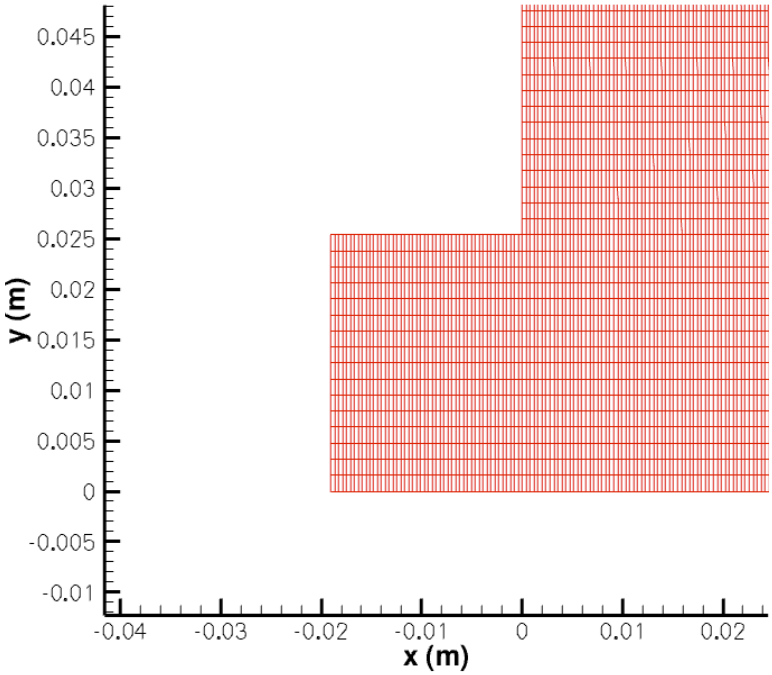

Figure 3.17: Zoomed view of combustor mesh showing speaker slit in x-y plane

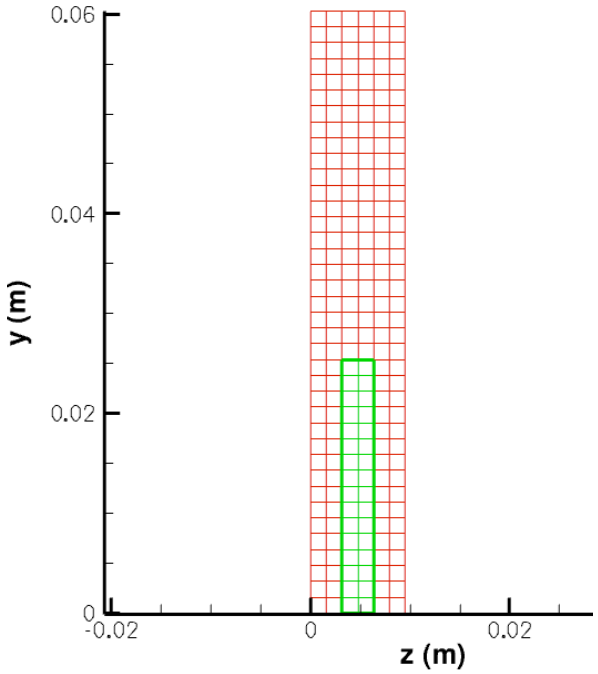

Figure 3.18: Zoomed view of combustor mesh showing speaker slit in z-y plane with speaker slit highlighted.

4. Cold Flow Results

4.1 Experimental Results

Previous work by Ghosh (2008) focused on performing cold flow studies using helium and air in place of hydrogen and oxygen. While this data provided a general point of comparison for the simulation validation, it did not allow for direct comparison with the hydrogen/oxygen based simulation results. Therefore it was necessary to perform acoustically forced mixing studies using hydrogen and oxygen.

From the previous results, it was seen that there were two primary conditions, a symmetric forcing case, which appeared to relate to forcing at a longitudinal mode of the system, and an asymmetric case, which appeared to be the result of forcing at a frequency not close to a resonant frequency. The symmetric condition occurred primarily in the 200-450Hz range, and the asymmetric case occurred at higher frequencies, roughly 700-900Hz. Two representative frequencies were selected for the experiments and simulations, one at 405Hz and the other at 885Hz. A baseline case illustrating the unforced flow field at velocities of 18/6/18 m/s is shown in Figure 4.1.

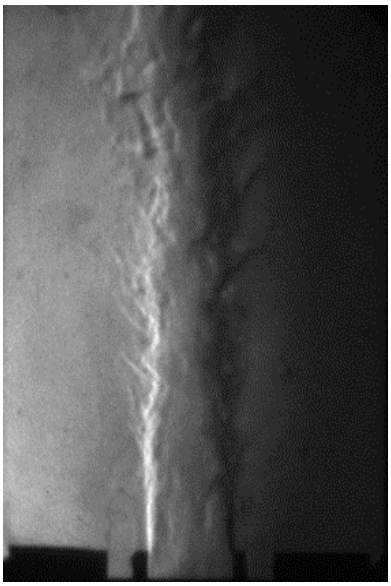

Figure 4.1 Schlieren image of unforced baseline H2/O2/H2 flow at 18/6/18 m/s

4.1.1 Acoustic Forcing at 405Hz

Figure 4.2 shows phase-locked images of forcing at 405Hz and 20vpp, with forcing provided from the left. The resulting flow field is very similar to what was seen using the helium-air mixture. For all of these cases, the velocities are calculated using a metering orifice and the assumption of choked flow, so that by setting a certain pressure in the gas line, a known mass flow rate and thus a known velocity can be achieved. However, since it was not possible to attain accurate velocity measurements at the hydrogen and oxygen inlets, it was assumed there may be some error in the exact velocity. Therefore, a case was also run at a calculated velocity of 27/9/27 m/s, representing a 50% increase in velocity. These results, shown in Figure 4.3, illustrate that a change in the velocity results in an expected increase in core jet length.

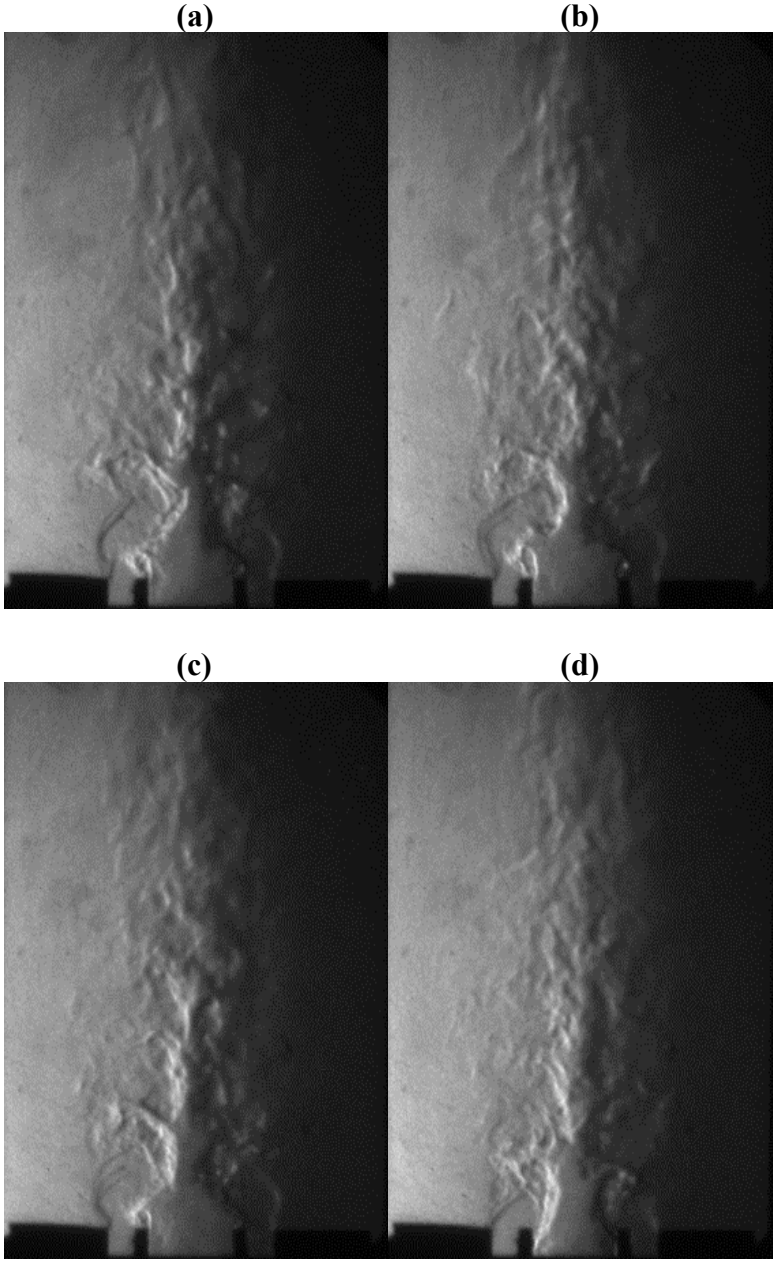

Figure 4.2: Phase-locked Schlieren images of H2-O2 flow with forcing at 405Hz and 20vpp (a) Phase= 0° (b) Phase = 90° (c) Phase= 180° (d) Phase= 270°

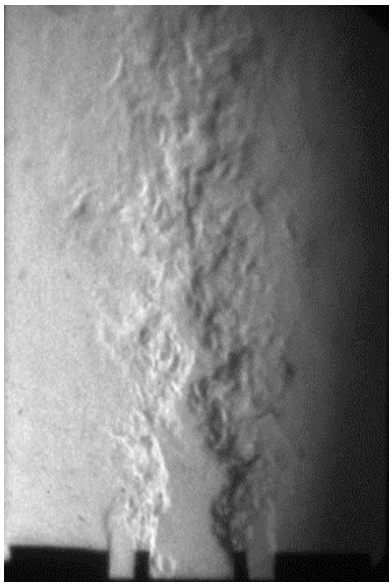

Figure 4.3: Schlieren image of H2-O2 flow at u=27/9/27 m/s with forcing at 405Hz and 20vpp

4.1.2 Acoustic Forcing at 885Hz

Next, forcing was applied at the higher frequency of 885Hz. The Helium-Air results had shown that for the travelling wave case, the resulting flow structure was highly dependent on forcing amplitude. Therefore for this frequency forcing was applied at a range of amplitudes, from 30vpp to 60vpp. Little effect on the flow field was seen at amplitudes less than 30vpp. Figure 4.4 shows phase-locked imaging of forcing at 885Hz and 60vpp. Unlike the 405Hz case, very little phase dependence is seen. Figure 4.5 shows the effect of ramping the amplitude from 30vpp to 60vpp, and shows that the flow begins to bend much more sharply as the amplitude is increased.

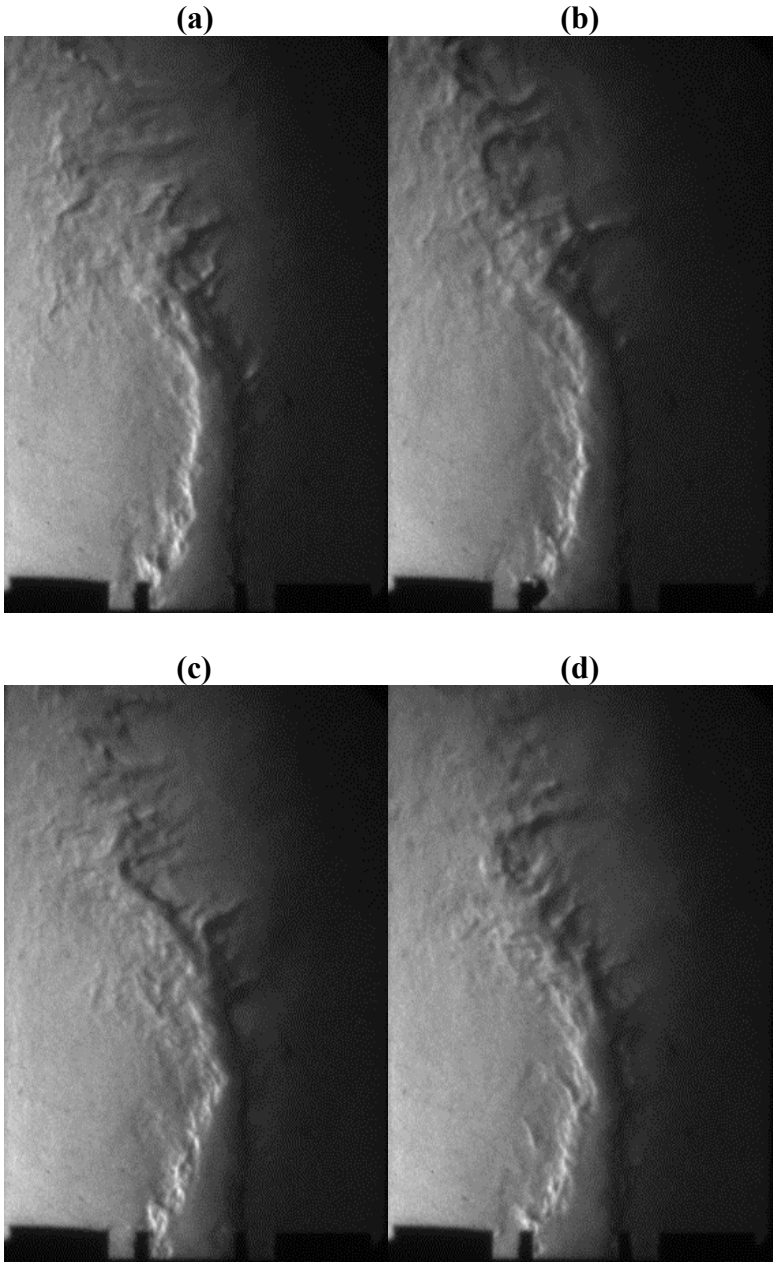

Figure 4.4: Phase-locked Schlieren images of H2-O2 flow with forcing at 405Hz and 20vpp (a) Phase= 0° (b) Phase = 90° (c) Phase= 180° (d) Phase= 270°

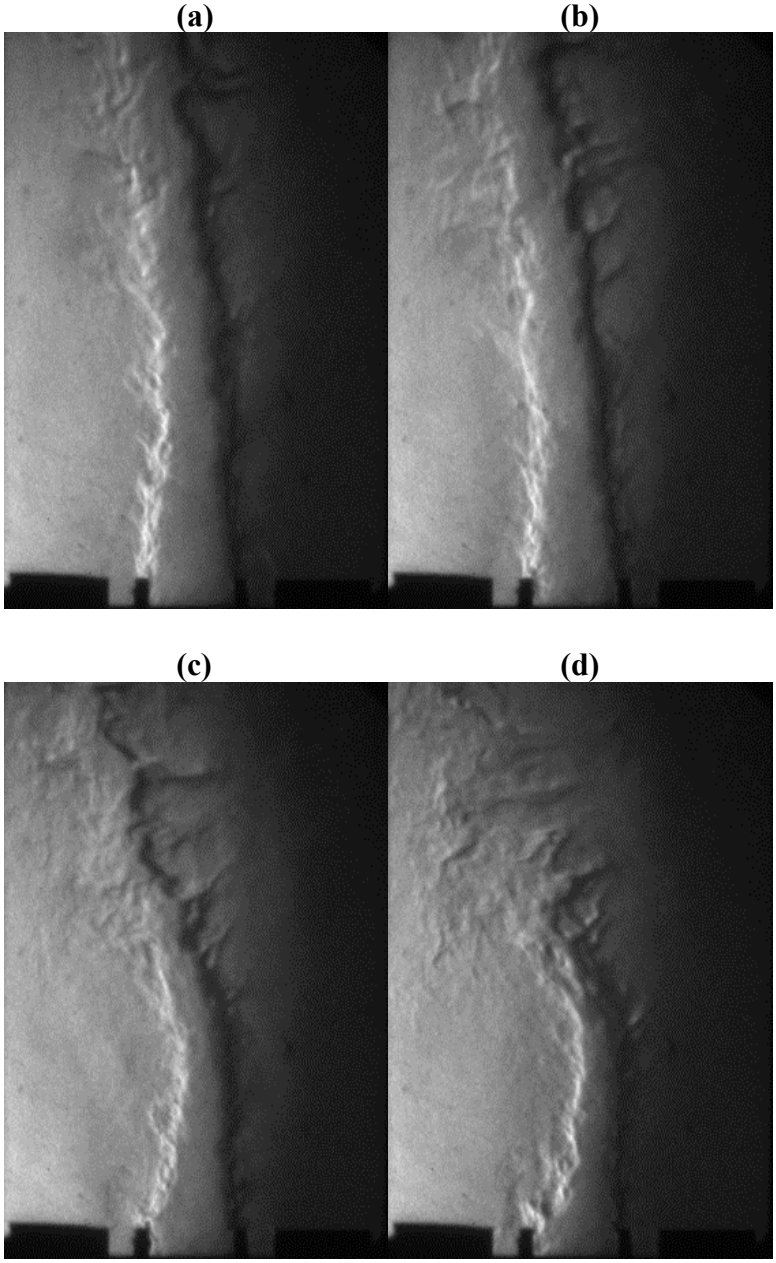

Figure 4.5: Schlieren images of H2-O2 Flow with forcing at 885Hz (a) 30vpp (b) 40vpp (c) 50vpp (d) 60vpp

Similar to what was done previously, a case was run at velocities of 27/9/27 m/s to observe the effect of errors in velocity estimating on flow structure. In this

case, forcing was provided at 885Hz and 60vpp. As shown in Figure 4.6, the higher velocity greatly decreased the bending in the flow.

Figure 4.6: Schlieren image of H2-O2 flow at u= 27/9/27 m/s and forcing at 885Hz and 60vpp

4.2 Simulation Results

4.2.1 Steady State Simulation

The first step in simulating the cold flow problem in Loci-CHEM was to generate an appropriate steady condition that could be used both as a point of comparison and as an initial condition file for acoustically forced simulations. Room temperature N_2 was used as the ambient condition for the combustor and plenum. A steady-state RANS simulation was run with H_2 and O_2 inflow activated and the numerical loudspeaker boundary set to a solid, viscous wall. Sufficient iterations were run to allow the inflow gases to convect through the combustor chamber and into the plenum and stabilize to a steady-state condition. Figure 4.7 shows the global results of the steady-state simulation. Figure 4.8 shows a zoomed view of the density

gradient in the near-injector region that shows the same region as the experimental images for use as a direct comparison.

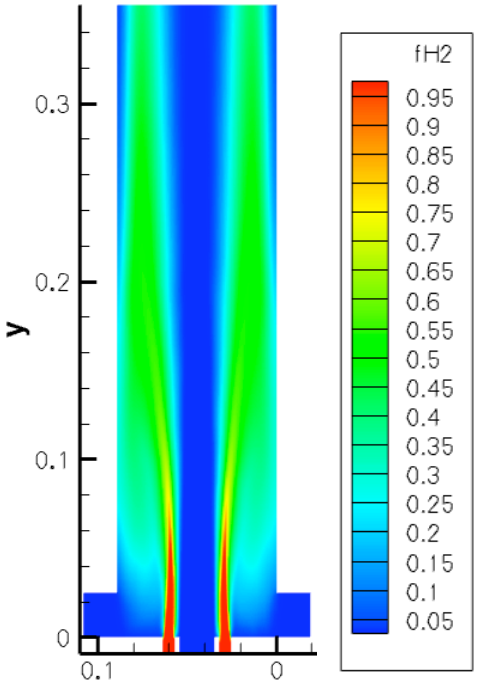

Figure 4.7: Baseline simulation for H2-O2 cold flow showing mole fraction of H2

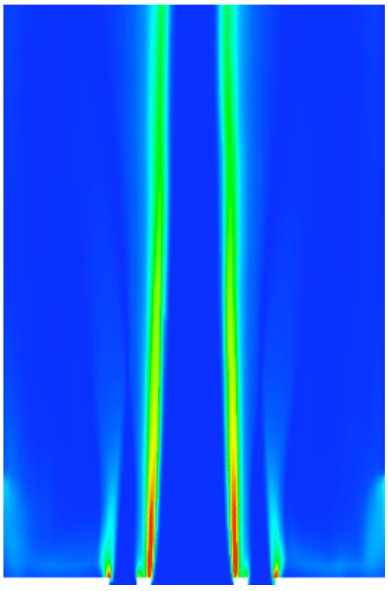

Figure 4.8: Zoomed view of near-injector field showing baseline density gradient magnitude

4.2.2 Acoustic Forcing at 405Hz

To apply acoustic forcing at 405Hz, the steady-state condition from the previous simulation was used as the initial condition for the forced simulation. A data file was supplied to the numerical loudspeaker boundary provided the specified time-dependent mass-flow to generate forcing at 405Hz and a velocity amplitude of u'=15 m/s. At this frequency, symmetric vortices generation was seen in the near-injector field. Figure 4.9 shows the density gradient in the near-injector field, and qualitatively agrees closely with the experimental results.

From acoustic analysis of the chamber, 405Hz is estimated to be approximately the 2^{nd} harmonic of the longitudinal mode running through the oxygen jet. Even though forcing is coming from only one direction, symmetric, in-phase oscillation is seen in the flow field. Looking at the streamlines from the phase-locked images in Figure 4.10, they strongly suggest that that the loudspeaker is being amplified by a longitudinal mode, and that this mode is affecting the mixing behavior in the near-injector region. Figure 4.11 shows pressure and velocity traces taken from the exit of the speaker slit. Velocity stays constant as expected, while pressure grows, further suggesting that acoustic resonance is occurring.

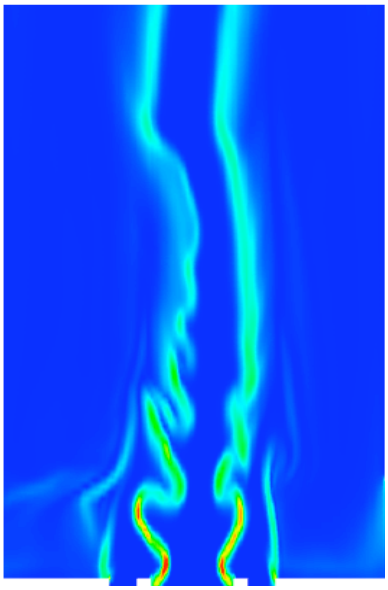

Figure 4.9: Zoomed view of near-injector field showing density gradient magnitude with forcing at 405Hz and u'=15 m/s

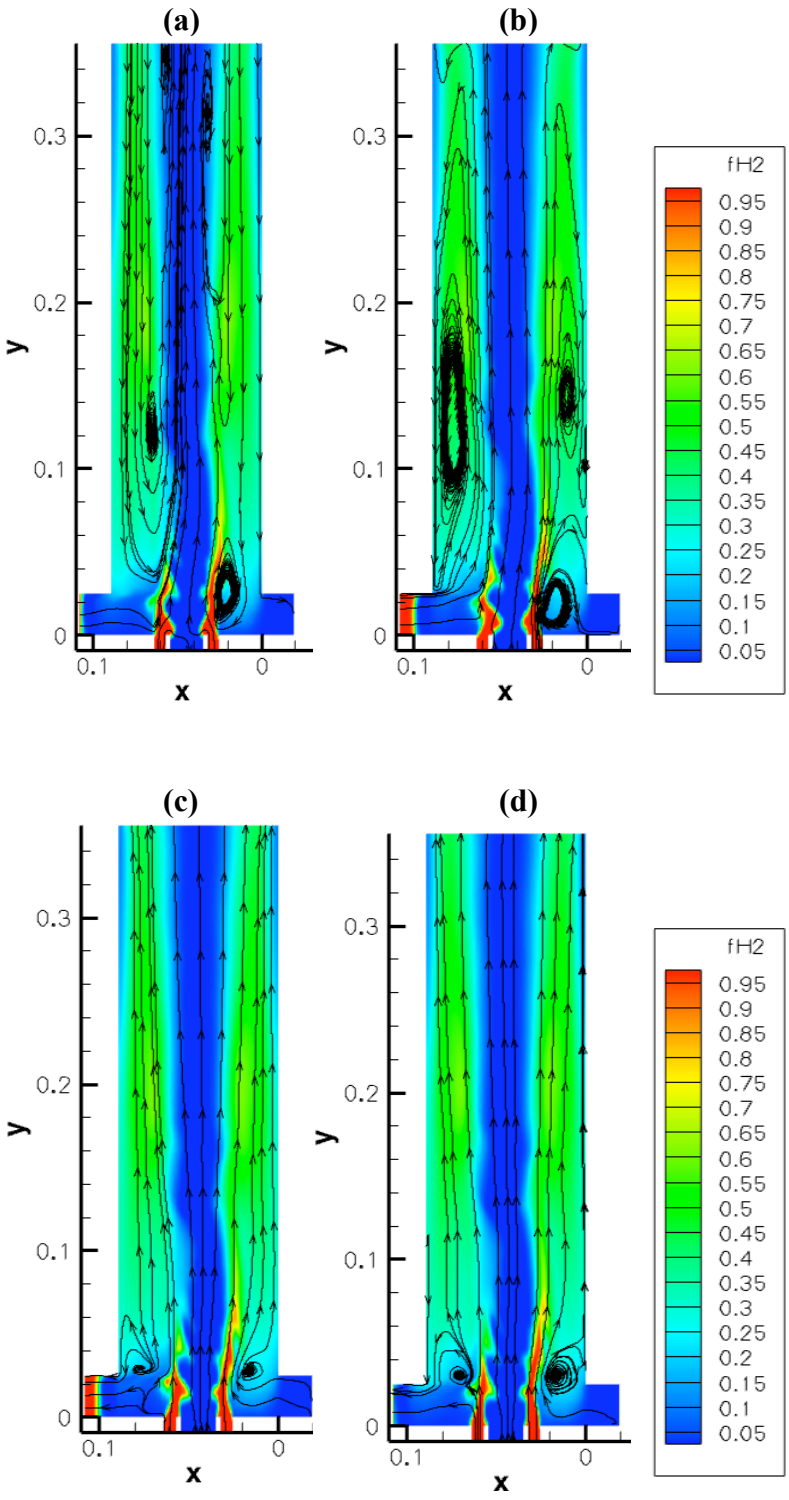

Figure 4.10: Mole fraction of H_2 and streamlines for cold flow simulation with forcing at 405Hz and velocity amplitude of 15 m/s
(b) phase=0°, (b) phase=90°, (c) phase=180°, (d) phase=270°

(a)

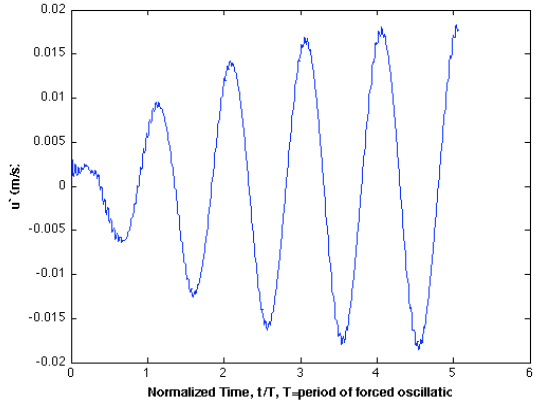

(b)

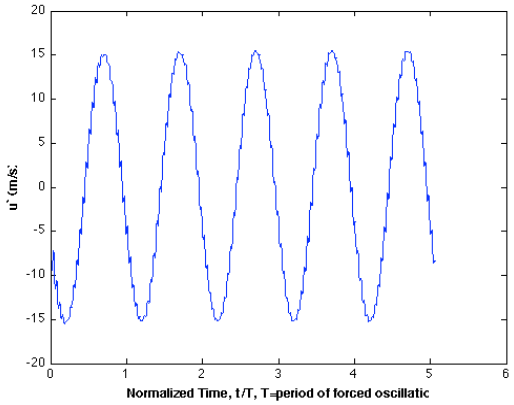

Figure 4.11: Time trace of normalized pressure and velocity fluctuations, forcing at 405Hz (a) P'/P fluctuations as function of number of forcing cycles, (b) Velocity fluctuations as function of number of forcing cycles

4.2.3 Acoustic Forcing at 885Hz

In addition to the symmetric response, a strong asymmetric response was seen in the higher frequency regime, and is believed to be associated with travelling, rather than standing, waves. Similar to the lower frequency case, the steady-state results were used as the initial condition before the time-dependent acoustic forcing at 885Hz was applied. The initial case was applied at an amplitude of u'=15 m/s, and showed slight

asymmetric interaction, with the flow bending towards the direction of forcing, although not very strongly. Figure 4.12 shows the density gradient in the near-injector field, which shows close similarity to the experimental result at the lower amplitudes. Figure 4.13 shows the phase-locked global view with streamlines, and it can be noticed that the far side of the flow field is largely unaffected by the forcing. Looking at the pressure and velocity fluctuations in Figure 4.14 near the speaker inlet, the velocity fluctuations once again remain constant, while the pressure fluctuation is dominated by noise, and does not grow in amplitude.

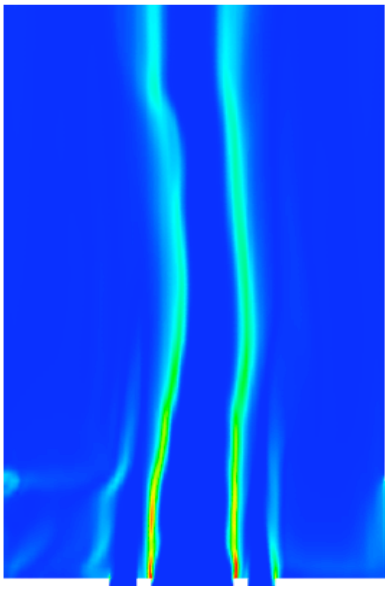

Figure 4.12: Zoomed view of near-injector field showing density gradient magnitude with forcing at 885Hz and u'=15 m/s

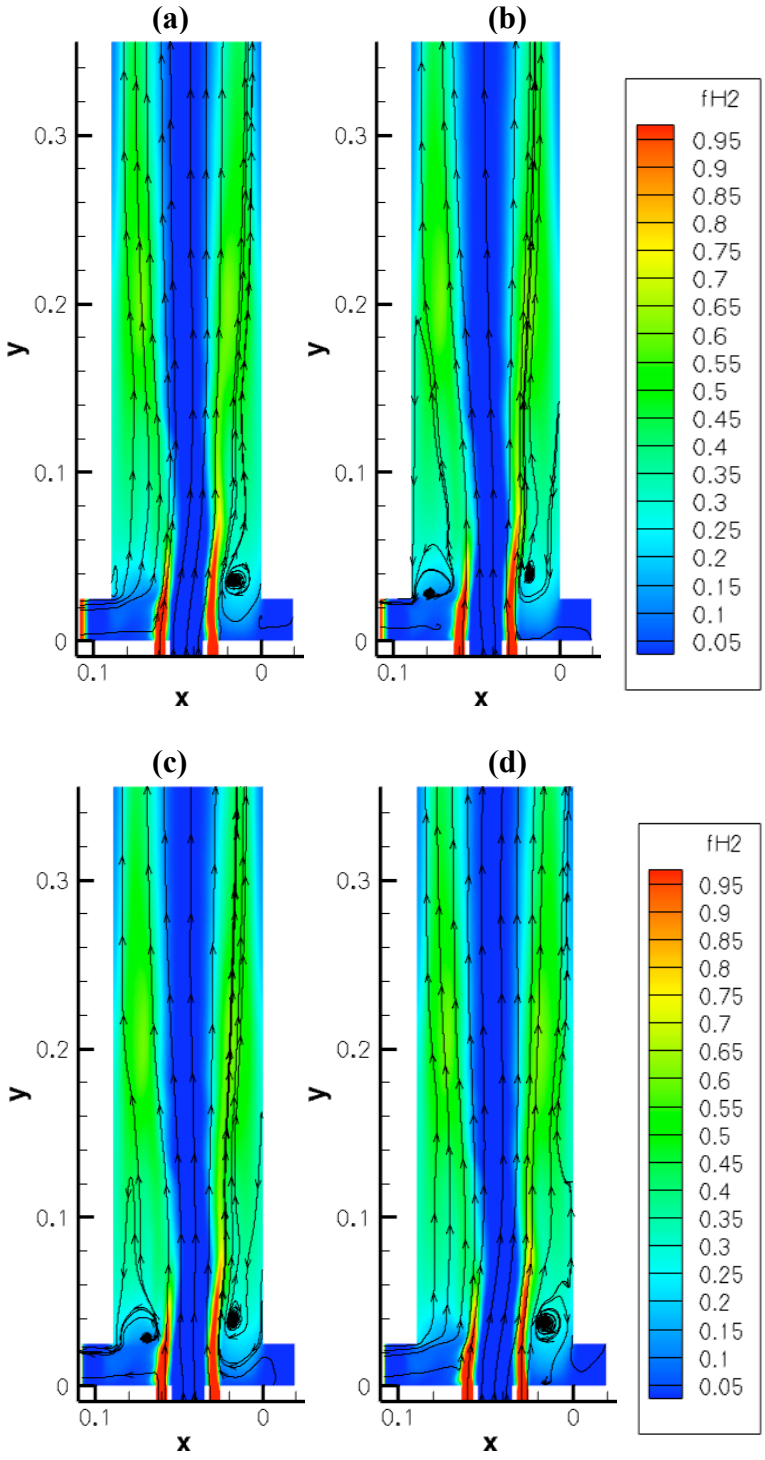

Figure 4.13: Mole fraction of H_2 and streamlines for cold flow simulation with forcing at 885Hz and velocity amplitude of 15 m/s (b) phase=0°, (b) phase=90°, (c) phase=180°, (d) phase=270°

(a)

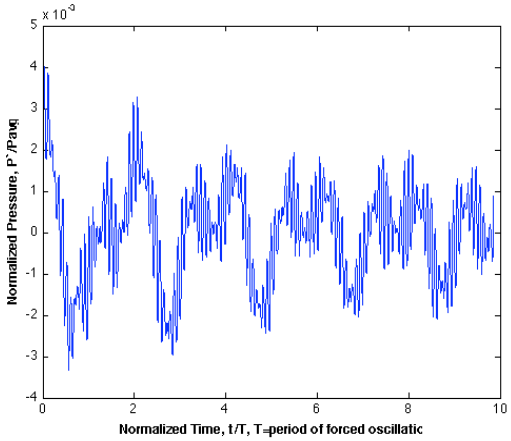

(b)

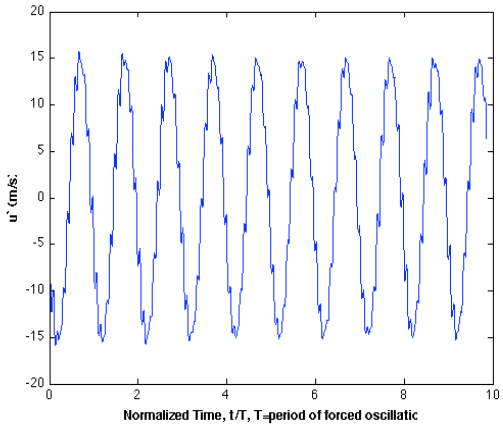

Figure 4.14: Time trace of normalized pressure and velocity fluctuations, forcing at 886Hz (a) P'/P fluctuations as function of number of forcing cycles, (b)Velocity fluctuations as function of number of forcing cycles

Doubling the forcing amplitude to u'=30 m/s shows significantly increased bending in the flow, as shown in Figures 4.15 and 4.16. This corresponds to the experimental results, although there is a longer delay before the flow bends back to the left than shown in the experiments. Additionally, at the higher amplitude much stronger vortices are formed on the near-speaker side, and a noticeable phase-dependence is seen in the global flow field, although the far side remains relatively

unaffected. Figure 4.17 shows the pressure and velocity traces, which show the increased amplitude in the velocity fluctuations with little change in the pressure fluctuations.

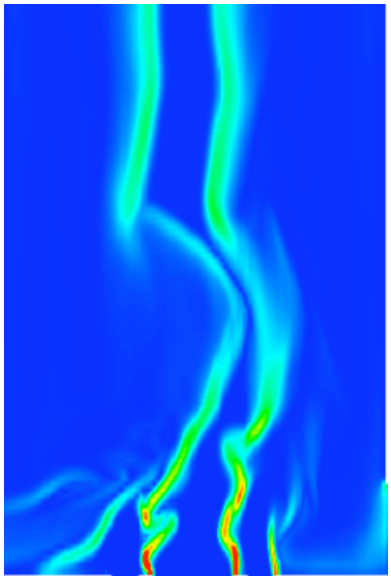

Figure 4.15: Zoomed view of near-injector field showing density gradient magnitude and forcing at 405Hz

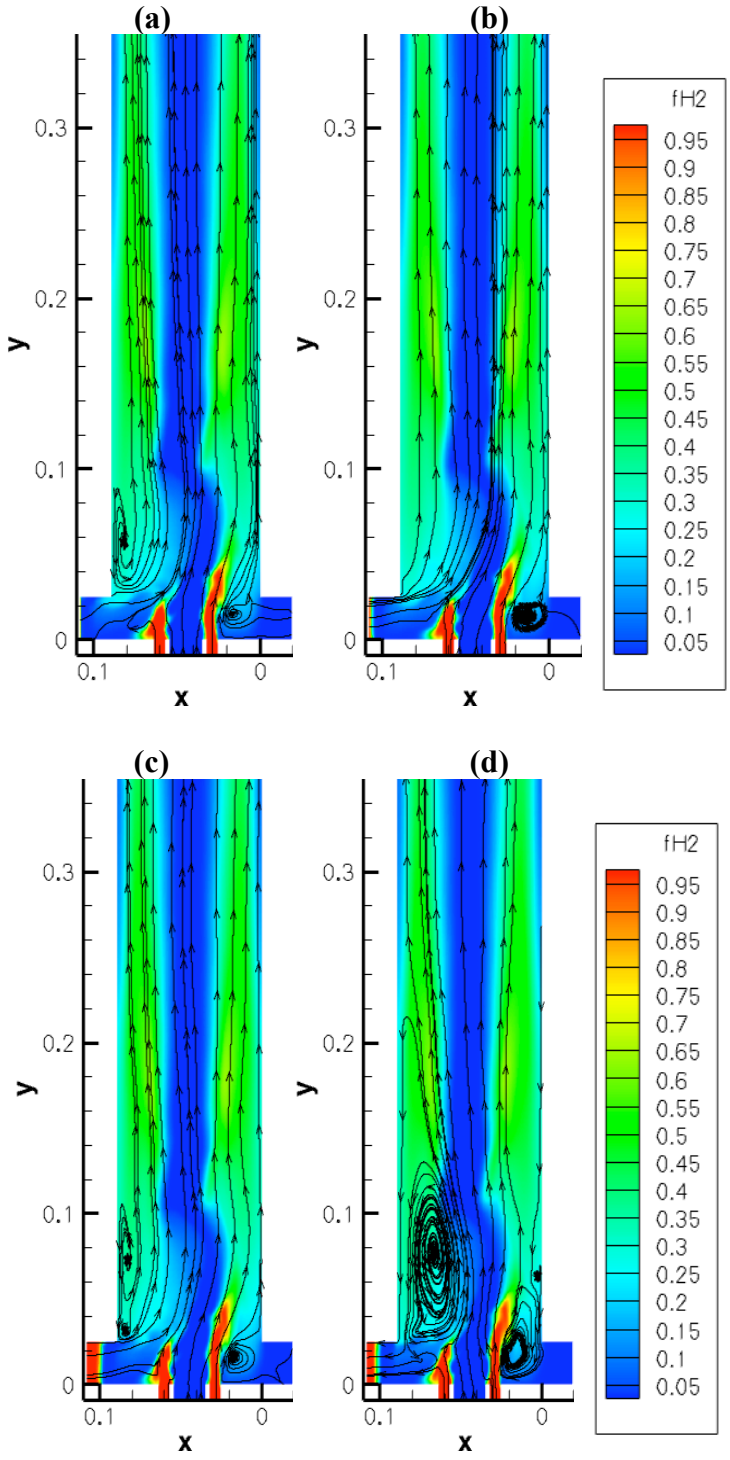

Figure 4.16: Mole fraction of H_2 and streamlines for cold flow simulation with forcing at 886Hz and velocity amplitude of 30m/s (b) phase=0°, (b) phase=90°, (c) phase=180°, (d) phase=270°

(a)

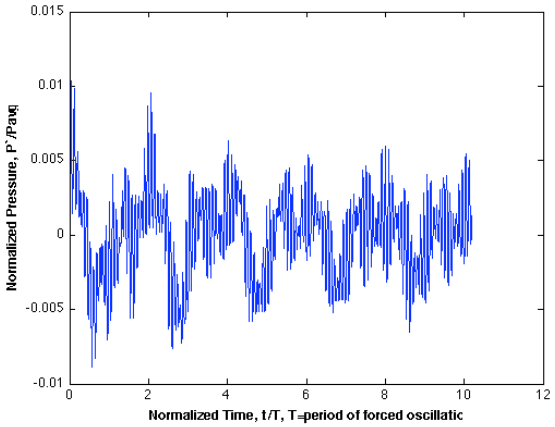

(b)

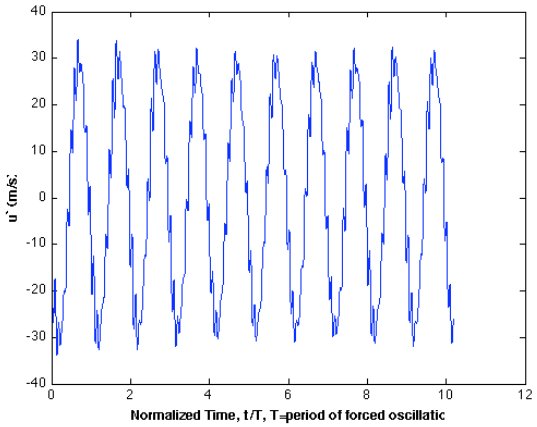

Figure 4.17: Time trace of normalized pressure and velocity fluctuations, forcing at 886Hz and high amplitude.

5. Reacting Flow Results

5.1 Experimental Results

Previous work by Ghosh [2008] demonstrated the effect of acoustic forcing on flames in a model shear-coaxial injector. Similar to the cold flow results, two distinct types of interactions were noticed, as shown in Figures 3.14 and 3.15. The low frequency forcing at 300Hz demonstrated a symmetric interaction, very similar to the cold flow interaction at 400Hz. However, at 1150Hz, instead of simply bending the flow, a strong asymmetric reaction was seen in which the speaker-side flame exhibited increased oscillatory behavior, while the far side flame remained stable. Also noticed as part of the original experiments was that the heat release oscillations were occurring at a frequency of around 97Hz, despite the initial forcing at 1150Hz. This suggests that some mechanism is coupling the forcing being felt in the near-injector field to the low frequency oscillations.

5.2 Simulation Results

5.2.1 Steady State Simulation

Similar to the process for the cold flow simulations, a reacting flow steady-state simulation was created to use as an initial condition for the acoustic forcing cases. Since the reacting flow simulations use a reacting H_2-O_2 chemistry set that does not contain nitrogen, it was decided to instead use room temperature H_2O gas as the ambient condition for the combustor chamber and plenum. Other boundary conditions were kept identical to the cold flow simulations.

In addition to the change in initial conditions, an ignition process also needed to be developed for the reacting flow simulations. Loci-CHEM provides a method for specifying an ignition source, although use of this feature for this case resulted in a failure to achieve convergence. Instead, an alternative method was used to establish a flame by increasing flow temperatures and then ramping back down to desired operating conditions. H_2 and O_2 inflow temperatures were set to 800K and allowed to mix normally until two stable diffusion flames formed. Inflow temperatures were then slowly ramped back down to 300K over several hundred iterations. As part of this process, it was discovered that it was necessary to use the time-dependent solver mode with a time step of less than 6 microseconds in order to maintain stability. For similarity with the previous acoustically forced simulations, a time step of 5 microseconds was used. Once the flame was established, several thousand iterations were required to allow the flow to convect through the combustion chamber and form stable flames.

Since OH* chemi-luminescence was used for the experimental imaging, OH mole fraction is displayed in the simulation results for comparison. Figure 5.1 shows the steady state simulation OH mole fraction, and Figure 5.2 shows the temperature plot for the steady state simulation.

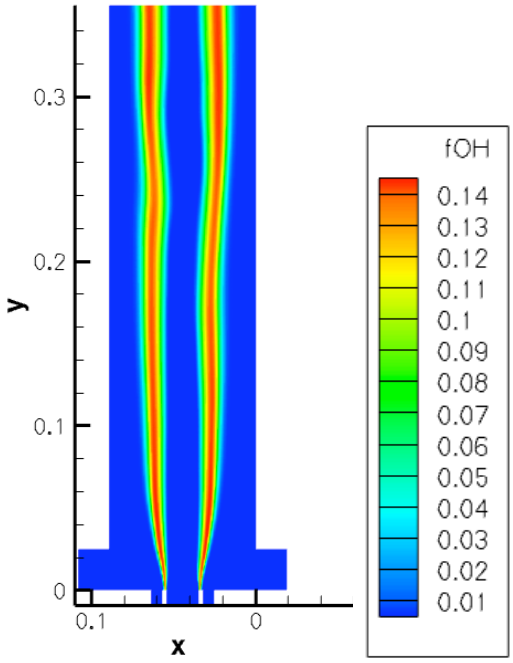

Figure 5.1: Mole fraction of OH for baseline reacting flow simulation

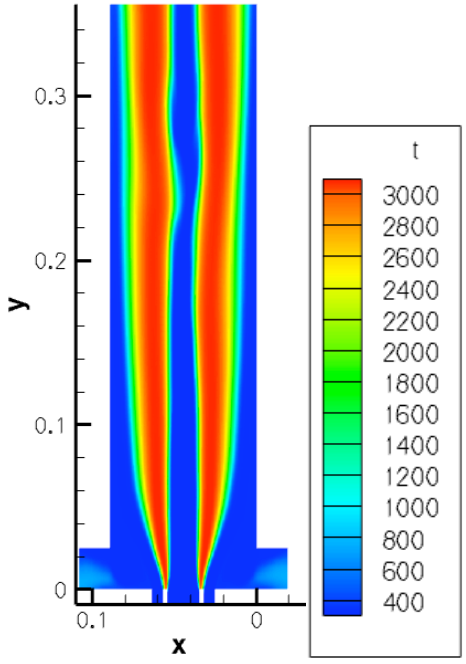

Figure 5.2: Temperature plot for baseline reacting flow simulation

5.2.2 Acoustic Forcing at 300Hz

Experimental white noise forcing results from the work by Ghosh[2008] shown in Figure 5.3 reveal that 300Hz corresponds to a peak in the spectral amplitude plot. This peak is believed to be associated with the quarter wave mode of the oxygen post. Ideally, a white noise simulation with reacting flow would have been run, similar to the white noise with air only case, the exceedingly long run times required to generate sufficient data made that option unfeasible. However, based on the previous acoustics only and cold flow simulations it was expected that the simulated combustor would display similar acoustic resonance characteristics with the reacting flow field. Initially, forcing was provided to the simulation at an amplitude of u'=15 m/s, with the results shown in Figure 5.4. Some ripple effects are seen in both flames, but not the strong oscillations seen in the experimental results. To help understand these results, probe data was taken at three locations in the near-injector field, as shown in Figure 5.5. Figures 5.6 and 5.7 show pressure and velocity traces at each of these probe locations, and while the velocity amplitude is constant, as expected, the pressure fluctuation is also at a constant amplitude, indicating that no acoustic resonance is occurring. This is different than what was expected and what was seen in the low frequency forcing for the cold flow results. Additionally, the pressure and velocity traces are seen to be quite noisy, with the noise occurring at a frequency of exactly 10kHz. Since the noise frequency is so clean, it is almost certainly artificial induced as an artifact of the discretization or numerical methods, however, the precise source has not yet been identified. Additionally, the noise

appears to damp out from the pressure oscillations as the signal travels away from the speaker, but shows inverse behavior in the velocity fluctuations.

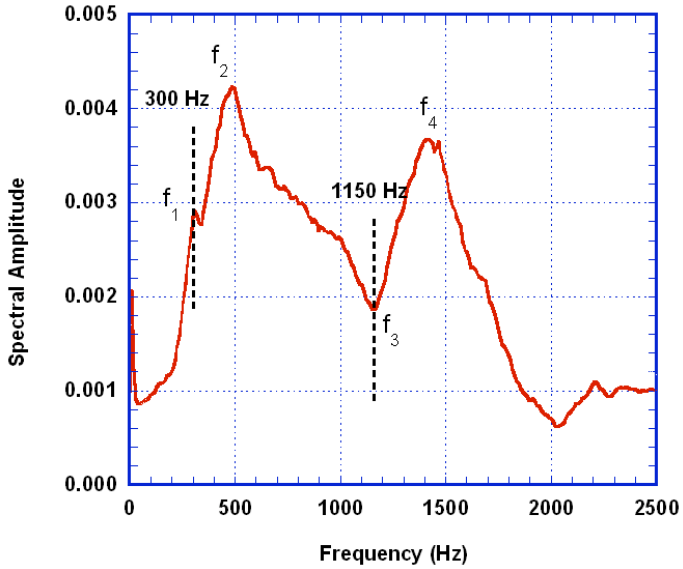

Figure 5.3: Experimental white noise forcing results for reacting H2-O2 flow

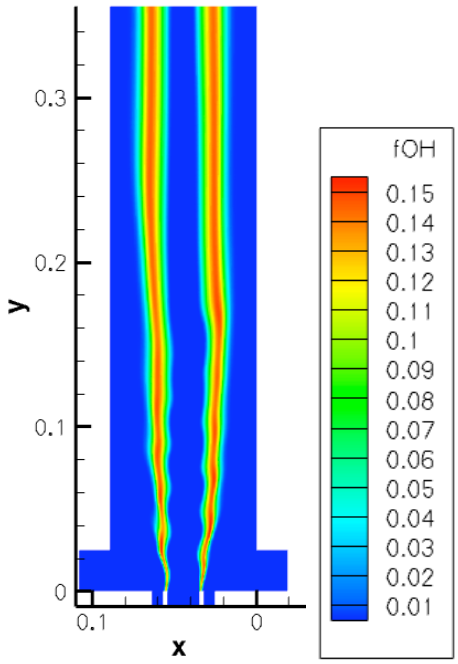

Figure 5.4: OH mole fraction for reacting H2-O2 flow with acoustic forcing at 300Hz and u'=15 m/s

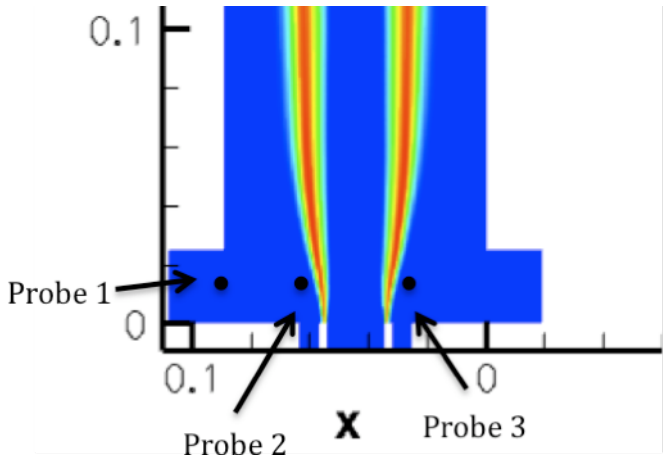

Figure 5.5: Zoomed view of near-injector region showing probe locations

(a)

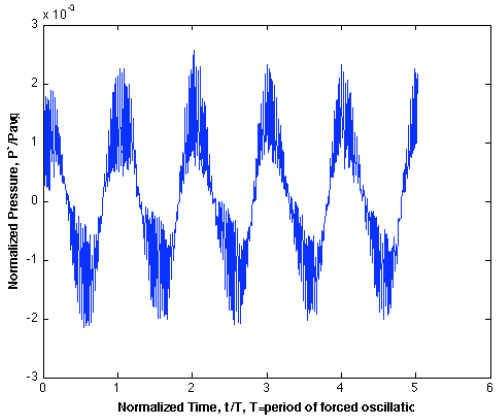

(b)

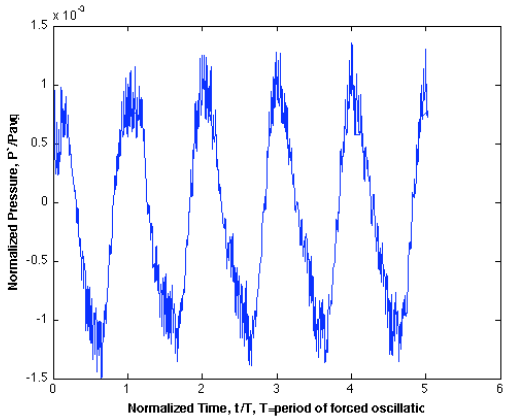

(c)

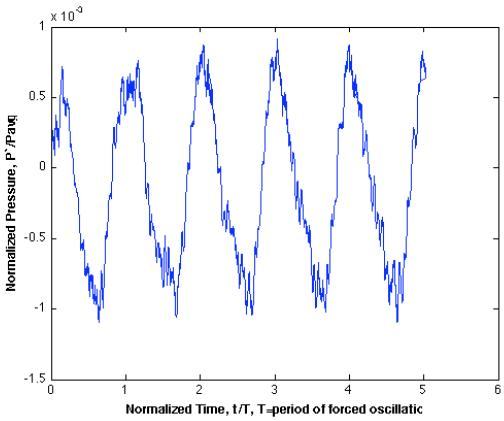

Figure 5.6: Pressure trace showing pressure fluctuations for reacting flow with acoustic forcing at 300Hz (a) Probe 1 (b) Probe 2 (c) Probe 3

(a)

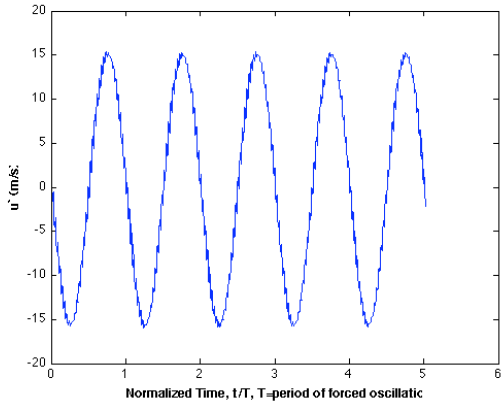

(b)

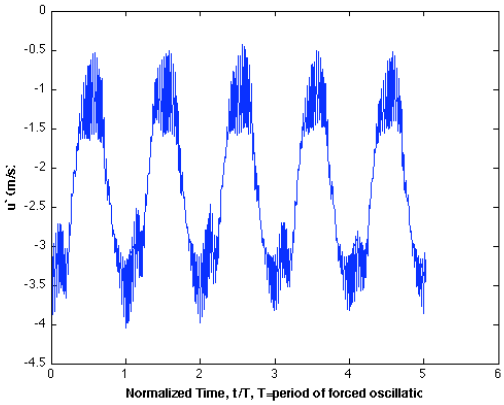

(c)

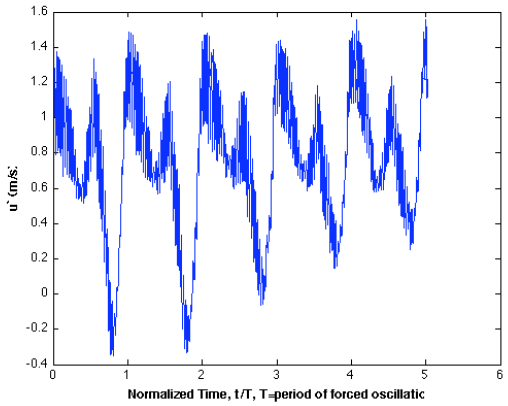

Figure 5.7: Velocity fluctuations for reacting flow with acoustic forcing at 300Hz (a) Probe 1 (b) Probe 2 (c) Probe 3

Since no acoustic resonance is occurring in the simulation, it suggests that the results will be amplitude dependent. A case was examined with the forcing amplitude increased to u'30 m/s. In this case, shown in Figure 5.8, the oscillations of the flame are stronger, although still not as well defined as the experimental results. Also, there is a noticeable phase delay between the left and right flame oscillations, which is not present in the symmetric oscillations seen in the experimental results.

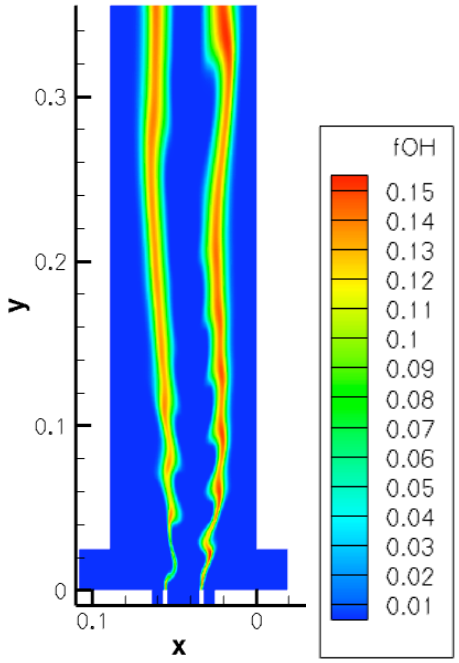

Figure 5.8: OH mole fraction for reacting H2-O2 flow with acoustic forcing at 300Hz and u'=30 m/s

5.2.3 Acoustic Forcing at 1150Hz

The high frequency forcing case displayed the most interesting characteristics during the experimental testing, and also is the most relevant case to actual combustion instability problems. However, when the 1150Hz forcing was applied to the reacting flow simulation, very little interaction was seen, as shown in Figure 5.9. Even as amplitude was greatly increased, no large-scale oscillations were seen. The near-injector field does show some similarity to the experimental results, in that the speaker-side flame shows a decrease in flame thickness, while the far side flame is shown expanded slightly; however, the strong heat release oscillations are not present. Figures5.10 and 5.11 show the pressure and velocity traces, which also a similar 10kHz noise that follows the same damping and growth pattern seen in the 300Hz simulation.

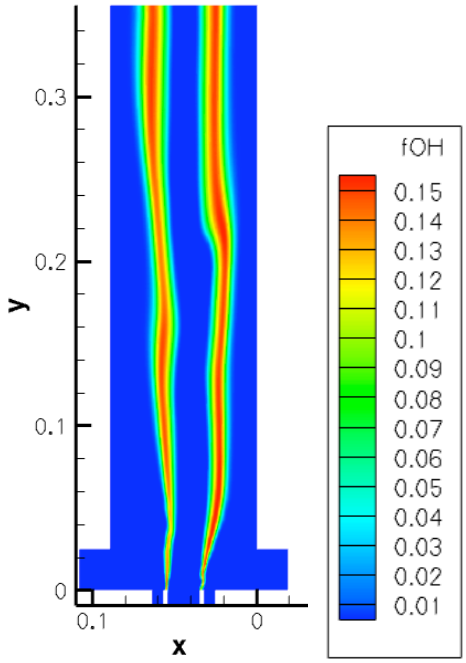

Figure 5.9: OH mole fraction for reacting H2-O2 flow with acoustic forcing at 1150Hz and u'=30 m/s

(a)

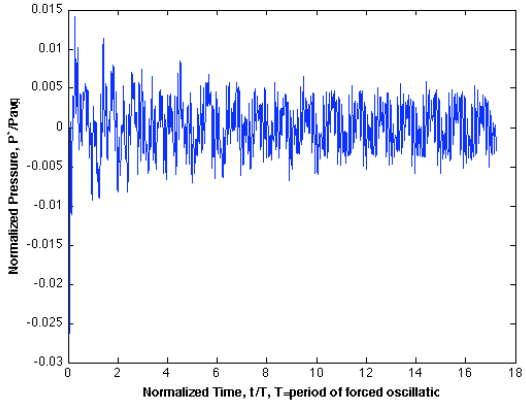

(b)

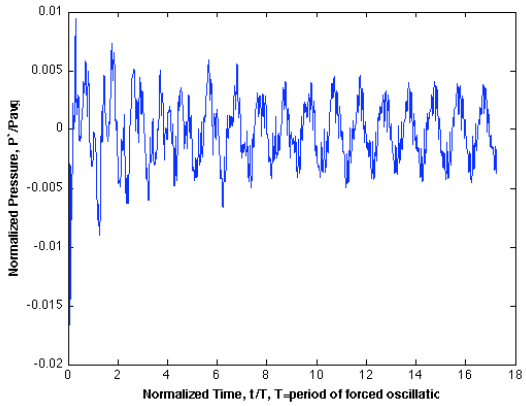

(c)

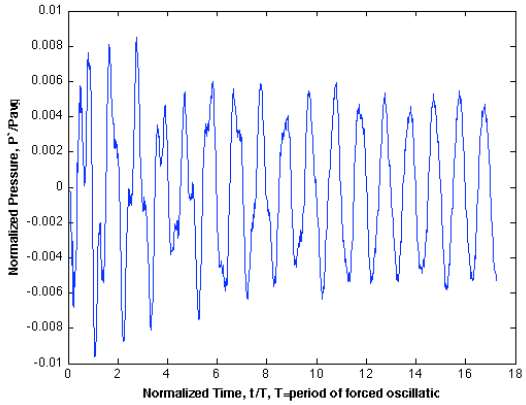

Figure 5.10: Pressure trace showing pressure fluctuations for reacting flow with acoustic forcing at 1150Hz (a) Probe 1 (b) Probe 2 (c) Probe 3

(a)

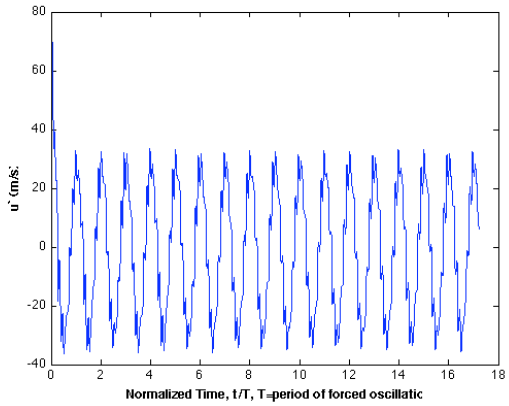

(b)

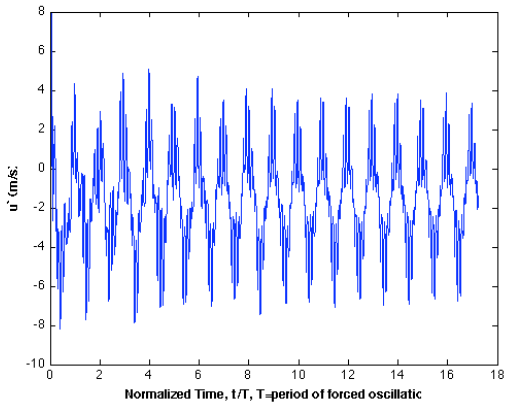

(c)

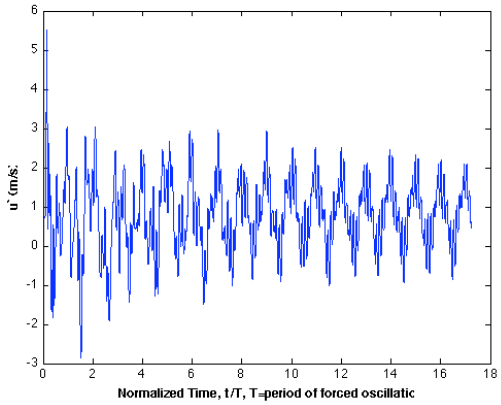

Figure 5.11: Velocity fluctuations for reacting flow with acoustic forcing at 1150Hz (a) Probe 1 (b) Probe 2 (c) Probe 3

In order to attempt to recreate the 97Hz large-scale oscillations seen in the experiments, the oxygen post mass flow rate was varied by 30% at a frequency of 97Hz to provide a source of that frequency. The 1150Hz amplitude was also increased by a factor of two, but this still failed to have a noticeable different effect on the flow field, as seen in Figure 5.12.

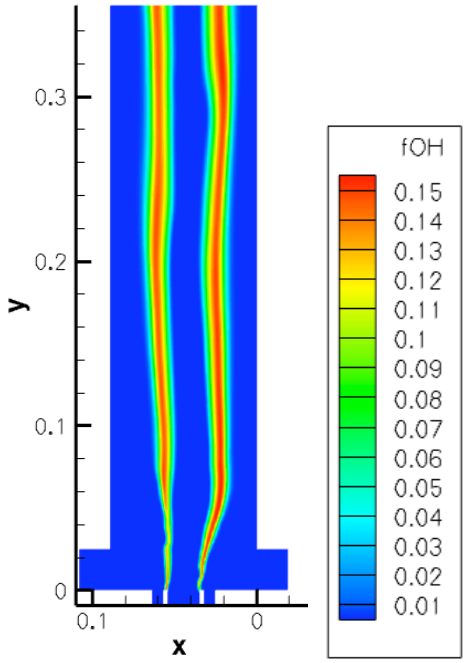

Figure 5.12: OH mole fraction for reacting H2-O2 flow with acoustic forcing at 1150Hz and u'=60 m/s and 30% O2 modulation at 97Hz

6. Summary and Conclusions

6.1 Grid Development

Basic verification studies were performed in Loci-CHEM and demonstrated the solver's ability to accurately resolve acoustic waves and acoustic resonance phenomena. A numerical loudspeaker boundary condition was developed to simulate controlled acoustic forcing. A computational mesh was then designed to emulate the physical model shear-coaxial injector. Grid refinement studies were conducted to define appropriate grid spacing. As the result of air-only white noise forcing simulations, the need to add a simulated plenum region was discovered, and an unstructured plenum was then added to the grid. Appropriate boundary conditions were selected to provide as optimal as possible simulation of the experimental setup.

6.2 Flow-Acoustic Interactions

Experimental results showed that there was strong frequency range dependence on the development of vorticity and on whether the resulting velocity interactions were symmetric or asymmetric. The simulation results from Loci-CHEM showed a similar dependence, with strong symmetric interactions occurring at 405Hz, and weak asymmetric interactions occurring at the higher frequency of 886Hz. Additionally, the higher frequency interactions increased as the amplitude of forcing was increased. By comparing numerical schlieren results to experimental schlieren images, conclusions could be drawn from the cold flow simulations with a high degree of confidence. Overall, Loci-CHEM demonstrated a good ability to simulate flow-acoustic interactions, and showed good agreement to experimental data.

6.3 Flame-Acoustic Interactions

Simulations of acoustically forced reacting flow did not show good agreement with the experimental data, especially in regard to the asymmetric flame wrinkling observed during the 1150Hz forcing conditions. Although some frequency dependence was seen, the low frequency interaction was not as strong or symmetric as expected, and no acoustic resonance was detected. At the higher frequency, the large oscillatory behavior seen in the experiments was not replicated in the simulations. It appears that the near-injector region shows the appropriate flow-acoustic interaction, but no strong coupling with the flame and heat release is seen.

6.4 Contribution

The contributions from this computational and experimental study are:

- Verification of Loci-CHEM's treatment of acoustics, and the development of a numerical loudspeaker boundary condition. This can allow for further validation and testing of Loci-CHEM.
- Development of a 3D grid modeling the experimental shear-coaxial injector rig. This model allowed for validation studies to be conducted and compared to the previously compiled experimental database
- Validation of Loci-CHEM with regards to flow-acoustic interactions with a non-reacting H_2-O_2 flow field. It was demonstrated that Loci-CHEM showed good qualitative agreement with experimental data, and demonstrated the appropriate frequency and amplitude dependencies. Additional experiments showing flow-acoustic interactions in a H_2-O_2 flow field were also conducted and added to the validation database.

- Assessment of Loci-CHEM's limitation on simulating flame-acoustic interactions under non-resonant conditions. The 3-D hybrid RANS/LES simulation, using the 6-species 8-reaction H2-O2 mechanism and the SST turbulence model, was unable to properly capture the asymmetric flame wrinkling behavior observed under acoustic forcing at non-resonant conditions. This is an ongoing work that requires further examination in the future.

6.5 Future Work

The work presented here offers many options where future studies may be directed. Primarily, continuing validation studies on reacting flow simulations in an attempt to identify the main causes of the discrepancies observed, especially in regard to the interaction between turbulent flames and traveling compression waves. More quantitative data for the proper time-dependant boundary conditions would be desirable from the experimental setup, particularly in the form of velocity, temperature, or pressure data at the compression driver and the propellant inlets. Additional validation of the combustor grid could be conducted for reacting flows which will help to eliminate possible sources of uncertainty in the mesh design. Additionally, for the reacting and cold flow simulations, if sufficient computational power is available, white noise forcing simulations could be conducted and compared to the existing experimental data, and help to identify differences in acoustic resonance behavior between the combustor grid and experimental setup. Alternatively, a wider rage of frequencies could be tested both experimentally and

using Loci-CHEM. This would allow for more points of comparison and also aid in identifying sources of error between the simulation results and experimental data. The author suggests three possible avenues of further research to help identify the reason for the discrepancies between the simulated and experimental reacting flow results:

- Computational grid resolution may need to be revisited for proper reacting flow simulation. The Kolmogorov length scale associated with the simulated flow conditions is around 100 microns, which is less than the grid spacing used but compensated for by the use of the SST turbulence model. This allows for a RANS/LES calculation to be performed rather than a direct numerical simulation (DNS). For the reacting flow simulations the flame thickness of the diffusion flame can be as small as 70 microns for simulated conditions. To provide full DNS resolution of the concentration gradients across the flame, a grid resolution of 10-15 microns would be required.. To avoid the excessive computational costs this grid spacing would require, a turbulent combustion model would need to be added to allow for proper flame simulation using RANS/LES-based grid sizing.
- Incorrect modeling of the combustor geometry could lead to inconsistencies between the simulation and experimental results. Although the grid was validated for white noise and cold flow tests, the acoustic impact of variables like inlet length and the effect of the exhaust duct may play a larger role in the flame acoustic interactions than in the cold flow results. This could lead to a shift in the frequencies where these phenomena are seen compared to the frequencies used in the experimental tests.

- Since the primary difference between the cold and reacting flow tests is a change in the chemistry model, the reacting flow model may not be appropriate for simulating the desired effects. The reacting chemistry model is a finite-rate chemistry model, and is optimal on DNS scaled grids. The larger grid sizes used in these simulations, coupled with the lack of a turbulent combustion model, may have led to the inability to simulate the oscillatory flame behavior. Improving the resolution of the grid or altering the chemistry model may reveal improved results for the reacting flow simulations.

Bibliography

Baker, L., Jr. and Steffen, F.W. (1958) "Screaming tendency of the gaseous-Hydrogen - liquid-Oxygen propellant combination," NACA-RM-E58E09.

Barrère, M., and Williams, F.A. (1969) "Combustion Oscillations in Industrial Combustion Chambers", Twelfth Symposium (International) on Combustion, The Combustion Institute, pp. 169-181.

Beam, R. and Warming, R., "An Implicit Factored Scheme for the Compressible Navier- Stokes Equations," AIAA Journal , Vol. 16, No. 4, April 1978, pp. 393–404.

Candel, S.M. (1992) "Combustion Instabilities Coupled by Pressure Waves and Their Active Control," Twenty-fourth Symposium (International) on Combustion, The Combustion Institute, pp. 1277-1296.

Crocco, L., Cheng, S.I. (1953) "High Frequency Combustion Instability in Rocket Motor with Concentrated Combustion," Jour. Am. Rocket Soc., vol. 23, no. 5, pp. 301-313.

Crocco, L., Cheng, S.I. (1956) Theory of Combustion Instability in Liquid Propellant Rocket Motors, AGARD monograph, No. 8, Butterworths Scientific Publications, London.

Culick, F. E. C. (1987) "A Note on Rayleigh Criterion," Combustion Science and Technology vol. 56, issue 4-6, pp.159-166

Culick, F., and Yang, V. (1995) "Overview of Combustion Instabilities in Liquid-Propellant Rocket Engines," Liquid Rocket Engine Combustion Instability, volume 169 of Progress in Astronautics and Aeronautics, pp. 3–37. AIAA.

Diao, Q., Ghosh, A., and Yu, K. H., (2008) "Acoustic Stability of Model Injector Flames Using H2-CH4 Fuel Mixture," AIAA Paper No. AIAA-2008-5251.

Ebrahimi, R., Mazaheri, K., and Ghafourian, A. (2000) "Mode Identification of High Amplitude Pressure Waves in Liquid Rocket Engines," Journal of Sound and Vibration, vol. 229, issue 4, pp. 973-991.

Ferraro, M., Kujala, R., Thomas, J., Glogowski, M., Micci, M. (1996) "Measurements of Shear Coaxial Injector Sprays – Cold Flow and Hot Fire Experiments" 32nd Joint Propulsion Conference, AIAA 96-3028

Ghosh, A. Diao, Q. and Yu, K. (2006)" Flame-Acoustic Interaction in GOX/GH2 Shear-Coaxial Injector Flow-field" AIAA-2006-762,Reno, NV

Ghosh, A. Diao, Q. Young, G. and Yu, K. (2006) "Effect of Density Ratio on Shear-Coaxial Injector Flame-Acoustic Interaction," AIAA-2006-4528, Sacramento,CA

Ghosh, A. Diao, Q. and Yu, K. (2007) "Experimental Investigation of Shear- Coaxial Injector Flame Stability on Flow Parameters", AIAA-2007-5569 , 2007, Cincinnati, OH

Ghosh, A., (2008)"The Role of Density Gradient in Liquid Rocket Engine Combustion Instability", Ph.D. thesis, University of Maryland, 2008.

Glogowski, M., Bar-Gill, M., Puissant, C., Kaltz, T., M. Milicic, M., and Miccit, M. (1994) "Shear Coaxial Injector Instability Mechanisms," AIAA-1994-2774
Williams, F.A. (1984) Combustion Theory, Benjamin Cummings, Menlo park, CA, 1984, second edition, chapter 9, pp. 294–372.

Harrje, D.T., and Reardon, F.H. (eds.) (1972) Liquid Propellant Rocket Combustion Instability, NASA SP-194

Hughson, M., Blades, E., Luke, E., (2007) "Analysis of Lattice Grid Tailfin Missiles in High-Speed Flow" 25th Applied Aerodynamics Conference, AIAA 2007-3932 Miami, FL

Hughson, M., Luke, E., (2008) "Unsteady Simulations of Missile Exhaust Plume Interactions" 26th AIAA Applied Aerodynamics Conference, AIAA 2008-6744, Honolulu, HI

Hulka, J. and Hutt, J. (1994) "Instability Phenomena in Liquid Oxygen/Hydrogen Propellant Rocket Engines," Liquid Rocket Engine Combustion Instability, volume 169 of Progress in Astronautics and Aeronautics, AIAA, pp 39-71.

Kim, J. S. and Williams, F. A. (1998) "Effects of non-homogeneities on the eigenmodes of acoustic pressure in combustion chambers," Journal of Sound and Vibration, vol. 209, no 5, pp 821-843.

Lang, W., Poinsot, T., Candel, S.M. (1987) "Active control of combustion instability," Combust. Flame, vol. 70, pp.281–289.

Luke, E. A., Tong, X.-L., Wu, J. and Cinella, P., (2004) "CHEM 2: A Finite-Rate Viscous Chemistry Solver – The User Guide," MSSU-COE-ERC-04-07, Mississippi State University, September, 2004.

Lin, J., West, J., Williams, R., Tucker, P. Chenoweth, J. (2005) "CFD Code Validation of Wall Heat Fluxes for a GO2/GH2 Single Element Combustor" 41st AIAA/ASME/SAE/ASEE Joint Propulsion Conference, AIAA 2005-4524 Tucson, AZ

Ma, T., Ghosh, A., Yu, K., Trouvé, A. (2006) "Numerical Investigation of Density Stratified Flow-Acoustic Interaction for Shear-Coaxial Injectors" 44th AIAA Aerospace Sciences Meeting AIAA-2006-0763, Reno, NV

Male, T. and Kerslake, W.R (1954) "A method for prevention of screaming in rocket engines," NACA-RM-E54F28A

Male, T., Kerslake, W.R., and Tischler, A.O. (1954) "Photographic study of rotary screaming and other oscillations in a rocket engine," NACA-RM-E54A29

McIntosh, A.C. (1991) "Pressure Disturbances of Different Length Scales Interacting with Conventional Flames," Combustion Science and Technology, vol. 75, pp. 287-309.

Oefelein, J.C. and Yang, V. (1997) "Analysis of Hydrogen-Oxygen mixing and combustion processes at high pressures," AIAA-1997-0798

Pariel, J.M., and Martin, L. S. (1969) "Contribution to the Study of Nonsteady-State Combustion in Industrial Hearths," Twelfth Symposium (International) on Combustion, The Combustion Institute, pp. 193- 201.

Rayleigh, L.J.W.S. (1945) The Theory of Sound, vol. 2. Dover Publications.

Reardon, F.,H. (1961) "An Investigation of Transverse Mode Combustion Instability in Liquid Propellant Rocket Motors," PhD Thesis, Princeton University.

Reardon, F.,H., Crocco, L., and Harrje, D.T. (1967) "Velocity effects in transverse mode liquid propellant rocket combustion instability," NASA-CR-80234

Richecoeur, F., Scouflaire, P., Ducruix, S., and Candel, S. (2006) "High Frequency Transverse Acoustic Coupling in a Multiple-Injector Cryogenic Combustor," Journal of Propulsion and Power, vol. 22 (4) 790-799.

Roy, C., Tendean, E., Veluri, S., Rifki, R., Luke, E., Hebert, S., (2007) "Verification of RANS Turbulence Models in Loci-CHEM using the Method of Manufactured Solutions" 18th AIAA Computational Fluid Dynamics Conference AIAA 2007-4203 Miami, FL

Selerland, T. and Karagozian, A.R. (1998) "Ignition, Burning and Extinction of a Strained Fuel Strip with Complex Kinetics," Combustion Science and Technology, vol. 131, issue 1 - 6, pp. 251-276.

Suzuki, M., Atarashi, T., and Masuda, W. (2007) "Behavior and Structure of Internal

Fuel-Jet in Diffusion Flame under transverse acoustic excitation" Combustion Science and Technology, vol. 179, issue 12, pp. 2581–2597

Strakey, P., and Talley, D. (2001) "Mixing Characteristics of Coaxial Injectors at High Gas/Liquid Momentum Ratios" AIAA Journal of Propulsion and Power, vol 17, No. 2

Summerfield, M. (1951) "A Theory of Unstable Combustion in Liquid Propellant Rocket Systems," ARS Journal, vol. 21, no. 5, pp. 108-114

Tsohas, J., Canino, J., Heister, S., (2007) "Computational Modeling of Rocket Injector Internal Flows" 43rd AIAA/ASME/SAE/ASEE Joint Propulsion Conference & Exhibit AIAA 2007-5571 Cincinnati, OH

Tsohas, J., Heister, S., (2009) "CFD Simulations of Liquid Rocket Coaxial Injector Hydrodynamics" 45th AIAA/ASME/SAE/ASEE Joint Propulsion Conference & Exhibit AIAA 2009-5387 Denver, CO

Tucker, P., Menon, S., Merkle, C., Oefelein, J., Yang, V., (2007)"An Approach to Improved Credibility of CFD Simulations for Rocket Injector Design" 43rd AIAA/ASME/SAE/ASEE Joint Propulsion Conference & Exhibit AIAA 2007-5572 Cincinnati, OH

Tucker, P., Menon, S., Merkle, C., Oefelein, J., Yang, V., (2008) "Validation of High Fidelity CFD Simulations for Rocket Injector Design" 44th AIAA/ASME/SAE/ASEE Joint Propulsion Conference & Exhibit AIAA 2008-5226 Hartford, CT

Veluri, S., Roy, C., Luke, E., "Comprehensive Code Verification for an Unstructured Finite Volume CFD Code" 48th AIAA Aerospace Sciences Meeting Including the New Horizons Forum and Aerospace Exposition, AIAA 2010-127 Orlando, FL

Wanhainen, J.P., Parish, H.C., and Conrad, E.W. (1966) "Effect of Propellant Injection Velocity on Screech in 20 000-Pound Hydrogen-Oxygen Rocket Engine," NASA TN D-3373.

Williams, F.A. (1985) Combustion Theory, 2nd Edition, Perseus Books Publishing.